Lawrence Berkeley Laboratory
UNIVERSITY OF CALIFORNIA

Materials & Molecular Research Division

CRYSTALLINE TO AMORPHOUS TRANSFORMATION IN SILICON

Suryanarayana Murty Cheruvu
(Ph.D. thesis)

September 1982

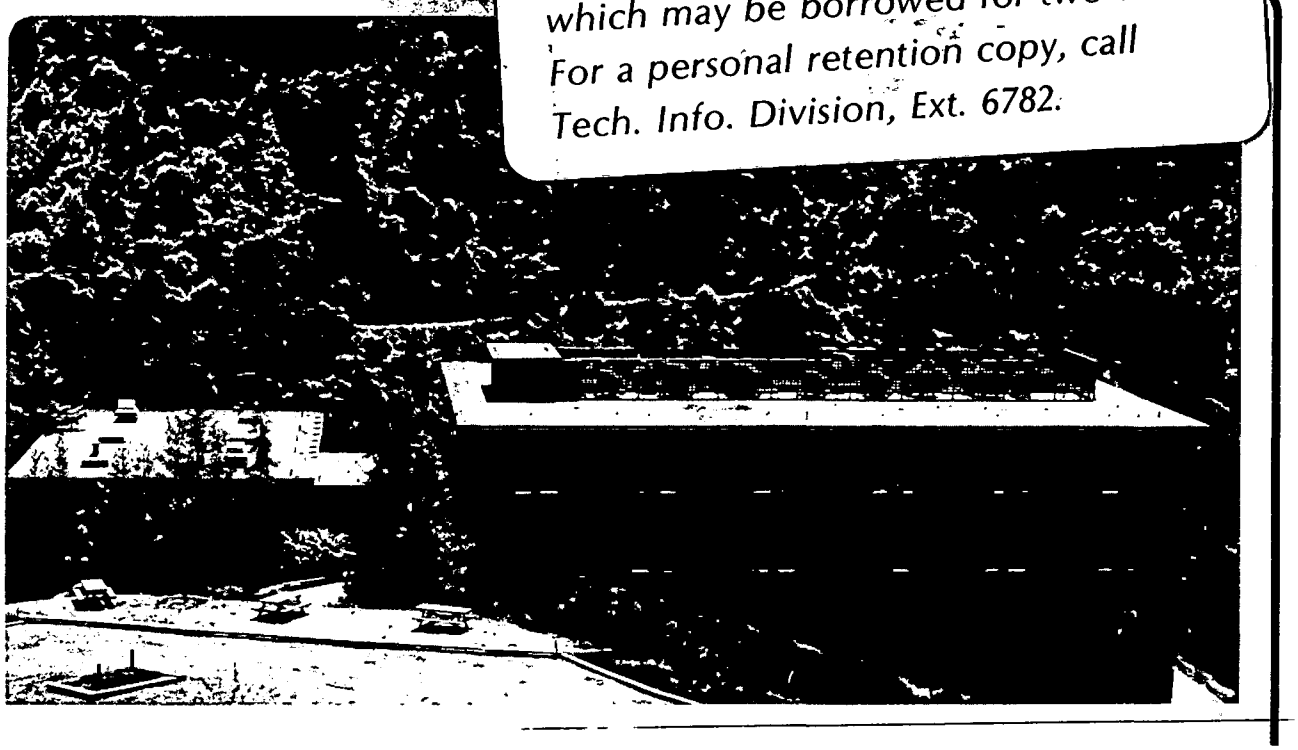

Prepared for the U.S. Department of Energy under Contract DE-AC03-76SF00098

DISCLAIMER

LBL-14923

CRYSTALLINE TO AMORPHOUS TRANSFORMATION IN SILICON

Suryanarayana Murty Cheruvu

(Ph.D. Thesis)

Materials and Molecular Research Division
Lawrence Berkeley Laboratory
University of California
Berkeley, California 94720

September 1982

This work was supported by the Director, Office of Energy Research, Office of Basic Energy Sciences, Material Sciences Division of the U.S. Department of Energy under Contract No. DE-AC03-76SF00098.

CONTENTS

CRYSTALLINE TO AMORPHOUS TRANSFORMATION IN SILICON

Suryanarayana Murty Cheruvu

(Ph.D. Thesis)

Materials and Molecular Research Division
Lawrence Berkeley Laboratory
University of California
Berkeley, California 94720

ABSTRACT

In the present investigation, an attempt was made to understand the fundamental mechanism of crystalline-to-amorphous transformation in arsenic implanted Silicon using high resolution electron microscopy. A comparison of the gradual disappearance of simulated lattice fringes with increasing Frenkel pair concentration with the experimental observation of sharp interfaces between crystalline and amorphous regions was carried out leading to the conclusion that when the defect concentration reaches a critical value, the crystal does relax to an amorphous state. Optical diffraction experiments using atomic models also supported this hypothesis. Both crystalline and amorphous zones were found to co-exist with sharp interfaces at the atomic level. Growth of the amorphous fraction depends on the temperature, dose rate and the mass of the implanted ion. Preliminary results of high energy electron irradiation experiments at 1.2 MeV also suggested that

clustering of point defects occurs near room temperature. An observation in a high resolution image of a small amorphous zone centered at the core of a dislocation is presented as evidence that the nucleation of an amorphous phase is heterogeneous in nature involving clustering or segregation of point defects near existing defects.

1. INTRODUCTION

It is well known that the technique of ion-implantation provides a powerful means of doping semiconductors.[1-10] However, for the conditions of practical importance, the damage that follows ion-implantation is severe.[11-14] An energetic ion comes to rest in a series of collisions with the electrons and nucleii of the target atoms. The major processes for energy loss are direct collision between the ion and the screened nucleus, excitation of electrons bound in the solid and charge exchange processes between the ion and the atoms in the target,[15,16]. If the energy transferred to the lattice atom exceeds a certain threshold energy, E_d, it will be displaced from its site. Normally one needs detailed information on the form of the differential scattering cross section, which is intimately related to the interatomic potential and the displacement probability function, to accurately calculate the extent of defect production.[17] Alternatively, Kinchin and Pease[18] developed a theory to estimate the number of atoms displaced by the implanted ion and the LSS theory[19] gives an approximate volume within which these displacements occur. Consequently, there is enough theoretical information to estimate the average defect density in any given damaged volume or cluster. The size and character of such clusters depend upon several factors such as mass and energy of the implanted ion, and mass and temperature of the target. If the defect density in the cluster reaches a critical value, one expects the cluster to be amorphous[18]; otherwise it is crystalline but rich in simple defects.[20]

1.1 Nature of damage clusters

Concerning the size and structure of the damage clusters, theoretical investigations have considered the crystal lattice structure, the atomic density, the cross section for secondary collisions and the thermal properties of the material surrounding the cascade region. As envisaged by Seitz and Kochler,[21] the lattice oscillations set-up in the wake of a recoiling lattice atom are approximately equivalent to rapid heating and quenching of a localized volume centered around the cascade region. This localized thermal pulse (temperature spike) has a life time of $\sim 10^{-11}$ sec. This concept was utilized to explain the presence of small damage clusters having liquid-like structure in deutron bombarded GaSb.

Brinkman,[22] in his displacement spike model of a cascade, has concluded on the basis of mean free path considerations that the size and structure of damage clusters will be determined not only by the purely thermal effect of the temperature spike but also by the transient chaotic atomic displacements and agitations produced in the cascade. Since the cross-section for displacement collisions increases as the moving ion slows down,[23] these spikes tend to form toward the end of the trajectory. This combination of thermal and athermal influences on the size and structure of the damage clusters has been studied by Parsons et al.[24] to account for the presence of small discrete crystallized regions observed in fast particle irradiated amorphous germanium.

Seeger[25] has suggested that the configuration of a damage cluster will also be sensitive to the crystal structure in which these

cascades occur. He postulated that the high energy collision process in the cascade should eject atoms into the surrounding crystal lattice. Some of these should travel long distances either as dynamic crowdions[26] and/or channelled atoms. This depleted zone, formed in the central region of the cascade by mass transport, has been illustrated by Beeler et al.[27] for damage production in iron.

Chadderton et al.[28] used channelling, Infrared (IR) absorption and transmission electron microscopy (TEM) to examine the damage produced in boron implants at room temperature and liquid-nitrogen temperature. They concluded that, in room temperature (R.T.) implants, fast moving point defects nucleate as clusters somewhat homogeneously, while at liquid-nitrogen temperature, the motion of these defects is arrested and the damage is "frozen in." The common understanding is that high temperature implants (> 500°K) do not produce amorphism even for high doses. In addition to temperature and dose, other factors such as energy dissipation by ionization, the effect of implanted species (e.g., B, P, Sb), the distribution of damage regions are also important factors affecting the crystallinity of these regions.[29]

1.2 Types of defects

The most prominant type of defect, reported in the literature, is the "Divacancy" in room temperature (R.T) implanted Silicon. Divacancies are stable at R.T. and were found in 200 keV Sb-implanted Silicon by Vook and Stein.[30] However, most divacancies are not formed directly but only as a result of vacancy migration, i.e., a large fraction of the divacancy population may be found outside the initially disordered region. In low temperature implants (80 90°K),

the formation of divacancies is inhibited by the low mobility of the vacancies.

1.3 Crystalline-to-amorphous (c → α) transformation

It is now appropriate to consider how the transformation from a crystalline phase to an amorphous phase takes place. There is little doubt that large numbers of atoms can be displaced by the projectile and that when this occurs in a sufficiently small volume, the characteristics of the material will change towards those of an amorphous material. Using the Richter and Brittling model[31] for amorphous germanium (α-Ge), in which tetrahedral bonding between individual atoms is maintained but one bond is stretched by 0.27 Å, Swanson et al.[32] showed that the increase in energy of the amorphous state over the crystalline state is 0.23 eV per elongated bond. This energy corresponds to a defect concentration of ~0.06 atomic fraction. Taking account of entropy changes, the same investigators showed that the Ge crystal containing a defect concentration of 0.04 atomic fraction should be unstable with respect to the amorphous state. From the point of view of ion-implantation, this can be taken as the lower limit. Recently Christel et al.[33] estimated that the Silicon lattice relaxes to an amorphous state when the defect concentration reaches about 10 percent at a temperature low enough to prevent long range diffusion of point defects.

In summary, the current ideas on the c → α transformation can be divided into two major phenomenological groups:[34]

(i) Models suggesting that the damage clusters are amorphous and that complete amorphization is considered to be the result of the accumulation and merging of individual amorphous clusters (heterogeneous character).

(ii) Models suggesting the formation of regions with high defect concentration, yet still crystalline until the defect concentration reaches some critical value, at which time the crystal becomes unstable and transforms to an amorphous state (Homogeneous character).

Some try to ascribe the first mechanism to heavy ions and the second, to light ions (e.g., Ref. 20).

1.4 Prior Related Research

The disorder production and c → α transformation were studied by several investigators using a number of experimental techniques such as optical reflectivity,[36] infrared absorption,[37,38] ion channelling,[39-41] electron paramagnetic resonance (EPR),[42-44] SEM electron channelling pattern,[45] transmission electron microscopy (TEM),[46-48] Hall effect[49] and carrier lifetime measurements.[50] In general, each of these techniques yields information about different aspects of the disorder. For example, optical absorption (1.8 μm divacancy) and EPR (Si-P3 center) measurements give information identifying the presence of specific defects. Optical reflectivity and EPR (isotropic center) can be used to evaluate the formation of an amorphous layer. Conventional TEM can give information on the size, morphology and depth

distribution of the disordered regions. Channelling measurements yield information on the depth distribution of the damage.

To mention a few noteworthy experimental investigations and criteria for distinguishing the amorphous state from the crystalline state, one can begin with the conventional TEM where electron diffraction shows a spot pattern for crystalline regions whose intensity and spacing depend upon Bragg reflection conditions. For a truly amorphous region, the spot pattern is replaced by concentric rings (called Debye-Scherrer rings). Davidson[51] used the TEM to study the c → α transformation in Sb implanted Si. Mayer et al.[52] used the He-backscattering technique in which the yield of the 1.2 MeV He^+ ions backscattered into a given solid angle is essentially the same for α-Si and crystalline Si, oriented in non-channelling directions. Unfortunately, the backscattering experiment measures an unknown combination of true lattice disorder and lattice strain. Stein[53] studied the transformation in Sb implanted Si using an optical absorption technique. Crystalline Si has a sharp optical absorption edge at a wavelength of 1.1 μm whereas amorphous Si prepared at R.T. by the glow discharge method has a very gradual absorption edge starting from 1.25 μm. A disordered region that is not amorphous will show a divacancy absorption band at a wavelength of 1.8 μm. Masuda[54] used the electron spin resonance (ESR) technique for studying the c → α through the development of divacancies. The experimental evidence, so far available, suggests that heavy ions such as Sb, As most likely produce a damage cluster containing both simple defects and regions with substantial amorphous content.

In the case of light ions such as carbon in Si and Ge, Hirvonen et al.[55] were able to show by a backscattering technique that a significant fraction of the disorder, measured at low doses of the implanted ion, could be attributed to lattice strain rather than major displacements. Westmoreland et al.[56] measured the dose required to form a continuous amorphous layer at -150°C and R.T. when boron is implanted in Si. Their results show that a dose of 1×10^{15} ions/cm^2 is sufficient at -150°C whereas a dose of 1×10^{17} ions/cm^2 is needed at R.T. This clearly indicates the importance of mobility of point defects in reducing the residual damage and nucleating the amorphous regions at heterogeneous sites. Optical absorption measurements by Stein et al.[53] for 400 keV boron implants and ESR experiments by Brower and Beezhold[57] support this point of view. It was therefore concluded that individual light ions produce only Frenkel pairs and the residual damage will depend upon various factors such as target temperature and types and densities of clusters that are available for nucleation of stable damage. The damage that follows the implantation of intermediate ions has characteristics that are intermediate between the heavy and light ions.

In spite of considerable experimental study, the mechanism of the $c \rightarrow \alpha$ transformation and the nature of individual damage clusters in ion-implanted layers of Si and Ge are still not completely understood. So far, an important point of debate has been whether the $c \rightarrow \alpha$ transformation occurs as a chance of aggregation of mobile point defects (Homogeneous type) or occurs as a formation of amorphous zones centered around the ion track with subsequent overlapping of these individual

zones (Heterogeneous type). Experimental results seem to support both possibilities. In addition, damage which depends on $(\text{dose})^{1/2}$ has been reported.[58,59] This dependence was attributed to the homogeneous model. On the other hand, the heterogeneous model was very successful[60] in predicting how the critical dose (ϕ^*) for complete amorphization depends on various parameters. However, the absence of comprehensive studies as regards the $c \rightarrow \alpha$ transformation in tetrahedrally-bonded semiconductors, in general, led to the development of several apparently incompatible phenomenological models.

1.5 Objective of Present Study

The objective of this present investigation is to understand the fundamental mechanism of the $c \rightarrow \alpha$ transformation by analysis of the c/α interface in Silicon, in particular, using High Resolution Electron Microscopy (HREM). Silicon was chosen because of its technological importance. The technique of ion-implantation provides good control over the degree of the damage by varying the relevant parameters. The specimen orientation, the preparation techniques and the implantation conditions were tailored to suit high resolution imaging requirements. A novel method for extracting information from the HREM negatives was also developed which is based upon the principle of microdiffraction using an He-Ne laser beam. This technique was used to analyze the nature of damage in different damage clusters. Also computer simulation of the lattice fringe image was done to study the effect of point defect concentration on the visibility of high resolution lattice fringe images. This kind of theoretical analysis, coupled with the optical microdiffraction from the TEM negatives as well as the

structural models generated with known point defect concentration, provided significant insight into the specific nature of the c/α interface.

2. THEORETICAL MODELS

Several theoretical models are available in the literature which are basically phenomenological and aimed at determining the critical dose (ϕ^*) required for c → α transformation. All these models can be categorized into two groups; one applicable to heavy ions and the other, to light ions. All the models applicable to heavy ions assume that the ions create a sufficiently large defect density around the ion track to ensure that the damage cluster is amorphous.

2.1 Gibbon's Model

A simple experimental dependence of damage build up on the dose (ϕ) was first shown by Gibbons[61] based upon the assumption that each ion produces an amorphous cluster and the c → α transformation takes place by overlapping of these individual clusters. The proper equation is

$$A_A = A_o \left[1-(1+A_i\phi)e^{-A_i\phi}\right] \qquad (1)$$

where A_A, A_o, A_i, and ϕ are total surface area covered by amorphous clusters, the total area being implanted, projected area of clusters on the surface and the ion dose respectively. Qualitatively, this provides a much more rapid approach to saturation once the conditions for the production of amorphous zones have become dominant. Gibbons extended his model for cases where n-tuple cluster overlap is required for the production of an amorphous zone, yielding

$$A_A = A_o\left[1 - \left(\sum_{k=o}^{k=n} \frac{(A_i\phi)^k}{k!} e^{-A_i\phi}\right)\right] \qquad (2)$$

He assumed no defect annealing which makes this a zero degree approximation.

2.2 Morehead & Crowder Model

Morehead and Crowder[61,62] proposed a model for continuous amorphous layer formation and estimated the critical dose required. They argue that a thermal spike surrounding the ion track dissipates in $\sim 10^{-11}$ sec leaving a highly disordered region of many broken bonds and displaced atoms. These displaced atoms reform bonds and change their positions to form a relatively stable phase in a time τ of $\sim 10^{-9}$ Sec. During this time, point defects escape via thermal diffusion from the disordered core surrounding the ion track. In Appendix III, the core is arbitrarily represented as a cylinder. The Outer sheath, whose width is δR, remains crystalline. The ultimate stable radius of the amorphous region is $(R_o - \delta R)$ and hence the number required for them to overlap and form a continuous amorphous layer is proportional to $(R_o - \delta R)^{-2}$. The critical dose, which is a function of temperature, is given by

$$\phi(T) = \phi(0)\left[1 - (2\tau D_v E_d N)\left(\frac{dE}{dx}\right)^{-1/2} e^{-E\, df/2kT}\right] \qquad (3)$$

where D_v, E_d, N, (dE/dx) and E_{df} are vacancy diffusion coefficient, displacement energy for a lattice atom, number of target atoms per cm^3, energy loss per unit length of penetration and activation energy for migration of a vacancy respectively.

The important factors for a given target material are nuclear stopping power of the ion, which determines R_o, and the temperature of the target, which determines δR. Dose rate is important when it is high enough to yield a steady state concentration of point defects in the crystalline material which is sufficient to retard the out diffusion of point defects. It is also important at temperatures when $\delta R \approx R_o$.

2.3 Vook and Stein Model

Vook and Stein[30] considered the effect of dose rate in their model. The defect concentration can be determined from the rate equation which contains a generation term proportional to the dose rate and a depletion term proportional to the above mentioned defect annealing. Vook and Stein predicted the critical dose required for the c→α transformation as

$$\phi(T) = \frac{n_o x}{N_o \left(1 + \frac{n_o k_o x}{\phi' N_o}\right) e^{-E_{df}/kT}} \ln \left(1 - \frac{n_c}{n_o}\right) \left(1 + \frac{n_o k_o x}{\phi' N_o}\right) e^{-E_{df}/kT} \qquad (4)$$

where n_o, N_o, k_o, ϕ' and n_c are ultimate defect density, number of defects created per ion, the rate constant, dose rate and the

critical defect concentration respectively. From this expression, it is possible to predict the critical dose (ϕ^*) assuming that when $n \rightarrow n_c$, a critical concentration of point defects, the material transforms to an amorphous state.

Dennis and Hale,[65,66] in an attempt to verify this model, conducted a series of experiments which detect the electron spin resonance (ESR) signal from the amorphous regions implanted with light ions (N^+) and heavy ions (K_r^+) at low (20 Kev) and high (180 Kev) implantation energies in Silicon at low (80°K) and high (~350°K) temperatures. No dose rate dependence was found and the temperature dependence was not as predicted by this model. Crowder[49] has found a dose rate effect for boron. His dose rate dependence was only for doses less than ϕ^*.

2.4 Webb and Carter Model

These researchers proposed a composite model involving all of the processes for amorphousness production and annealing.[67,70] In their composite model, an assumption is made that each ion around its track creates a number of regions with different disorder densities. Mainly three regions were defined. A_u, as yet undamaged, A_d, damaged but not amorphous and A_A, amorphous. The region A_d was further divided into M different regions of differing defect density. Associated with each region is the damage cross-sectional area a_A, a_d (which is sub-divided into a_1, a_2, . . . a_M). Upon further irradiation, overlap of newly generated damage with different existing damage densities causes promotion to higher defect density regions until a region is promoted higher than the critical M^{th} region when it becomes

becomes part of the amorphous region. Annealing was also considered to occur during irradiation. Three different time constants were considered to represent the different rates of annealing in different regions. τ_A is the time constant associated with amorphized zone. The region A_d was sub-divided not by defect density but by two different types of disorder which have two different annealing rates. This is not unreasonable if one assumes a region containing both simple defects and more complex defects, the annealing behavior of which will be quite different. Thus, a region A_d' containing simple defects will possess an annealing time constant τ' and a region A_d'' containing defect complexes will possess an annealing time constant τ''. With these assumptions, Webb and Carter[67] set up a set of coupled differential equations to describe the time dependence of disordered area generation rates and solved for the fractional amorphized area A_A/A_o in terms of dose ϕ where A_o is the total area. The equations are not presented here due to their complexity. Using this model, they could show the effects of dose rate thus giving some indications as to the disordering mechanism leading to the amorphous production.

2.5 Chadderton's Homogeneous Model

When light ions such as boron are implanted, the damage clusters consist principally of simple Frenkel Pairs whose density increases to a substantial value only near the end of the ion track. At the beginning of its trajectory, the electronic stopping power for boron in Si is ~0.02 kev/Å while its nuclear stopping power is only 0.002 kev/Å. Electronic stopping power, therefore, dominates until the energy of the

projectile is reduced to 20 kev. In such a case, the damage that is stable at room temperature is rarely produced directly by the projectile but only by subsequent diffusion of point defects to damage nucleation sites. Such a process is called homogeneous nucleation as opposed to the heterogeneous nucleation that takes place spontaneously in a heavily damaged region. Homogeneous nucleation of damaged clusters is generally characterized for short periods by a linear dependence of the state of disorder on ion dose followed by a longer period during which the disorder is proportional to $(\text{dose})^{1/2}$. This $(\text{dose})^{1/2}$ dependence seems to be a fundamental characteristic of homogeneous nucleation.[71,72]

In the particular case when M_1, Z_1 and M_2, Z_2 (the mass and atomic number of the ion and target atoms) are small, large cascades occur only rarely and primary and higher-order knock-ons generate only a few small groups of displaced atoms. Such conditions discourage the formation of amorphous zones by a displacement spike ;or depleted zone mechanism. One might expect a fundamentally different nucleation behaviour when light ions are implanted. This difference may be exaggerated at elevated temperatures if the point defects can readily migrate. Therefore, for light ions implanted in Si and Ge at room temperature, the basis of the model is homogeneous generation of point-defects. Chadderton, in his model, assumes that (i) a ;constant homogeneous concentration of interstitials are generated per unit time during implantation and (ii) interstitials can interact with the homogeneous distribution of vacant lattice sites, nucleation traps,

saturable traps and unsaturable traps. The most appropriate differential equations are

$$\frac{dn_s}{d\phi} = \frac{N_o}{N} (N_s(0) - N_s) \tag{5}$$

$$\frac{dn_u}{d\phi} = \frac{N_o}{N} N_u(\phi) = \frac{N_o}{N} N_u(0) \tag{6}$$

$$\frac{dn_n}{d\phi} = \frac{N_o}{N} (N_n(0) - \gamma n_n) \tag{7}$$

$$\frac{dn_i}{d\phi} = \frac{N_o}{N} (N - n_i) \tag{8}$$

where N_s, N_u, N_n, n_s, n_u, n_n are the number of saturable traps, unsaturable traps, nucleation sites and the number of interstitials trapped at these sites per unit volume respectively. The parameter γ is an arbitrary one and N is the sum of $N_s(\phi)$, $N_u(0)$, $n_i(\phi)$, $N_n(0)$ and $\gamma n_n(\phi)$. It is easy to solve these equations for a particular case where unsaturable traps are dominant and the influence of other traps is negligible. Chadderton obtained the solution for the instantaneous concentration of interstitials $n_i(\phi)$ as a function of dose and showed that $n_i(\phi) \propto (\phi)1/2$ which explains the basic $(\phi)^{1/2}$ dependence of the damage. When n_i reaches a critical concentration n_c, the c→α transformation takes place. The main purpose of Chadderton was to demonstrate that the $(\phi)^{1/2}$ dependence of implantation-induced disorder by light ions in Silicon is a characteristic feature of nucleation at traps. Such a dose dependence

reflects the early stages of point defect clustering (true homogeneous nucleation) during irradiation and through simultaneous existence of monomers, dimers, trimers and higher order interstitial aggregates. It was explained that this $(dose)^{1/2}$ dependence itself is, in some degree, a direct consequence of the constant capture cross section of unsaturable traps.

2.6 Energy Deposition Model

Vook[73] proposed a simpler criterion for the c→α transformation based upon their observation of critical doses for various ions (B, P, Sb) at lower temperatures. They found the critical doses to be independent of temperature at the lower temperature range from 100°K to 200°K. This can be true since at lower temperatures, nearly all of the damage produced will be stable and therefore the amorphousness can be predicted from the knowledge of energy deposition per unit volume which is the product of nuclear stopping power (kev/cm) and dose (ions/cm^2). They estimated, on this basis, that if the target temperature is such that all the damage is stable, the energy deposited should be of the order of 10^{21} kev/cm^3 for any ion. This was interpreted as a phenomenon akin to melting that occurs in the formation of amorphous material.

3. COMPUTER SIMULATION OF LATTICE IMAGES

An important consideration concerning the c→α transformation is the critical point defect concentration and the influence of this concentration on the existence of identifiable crystalline order. The disappearance of lattice structure, characteristic of crystalline order, would be expected to be gradual if the amorphous state were to be reached simply by increasing the point defect concentration until the critical density was reached. Before this happens, there may be a sudden transformation to the amorphous state. This would lead to a sharp interface with a thickness comparable to atomic dimensions between small amorphous zones surrounded by crystalline material and between small crystalline regions surrounded by amorphous material. This aspect will be discussed again in detail later. In order to understand the nature of the c/α interface, whether it is sharp or diffused, it is necessary to simulate the appearance of the lattice fringe structure in a HREM lattice fringe image with known point defect concentration.

A very useful feature of high resolution electron-optical images is that when they are taken under certain well defined conditions,[74,78] they represent a projection of crystal potential along the incident electron beam direction. Computer simulation of lattice fringe images involves calculation of real space amplitudes and hence the intensity of the electron wave function $\psi(x,y)$ at the exit surface of the specimen which is directly related to the crystal potential.

Based upon a physical optics approach to the diffraction problem, Goodman and Moodie[79] developed a computing technique which enables the intensities of diffraction patterns or electron microscope images to be calculated with arbitrary accuracy by integrating the effects on a wave transmitted through a crystal. The crystal is treated as a series of n scattering slices (multi-slice approach) cut in the direction perpendicular to electron beam direction on to which the potential from the slice between Z and (Z+ΔZ) is projected, separated by vacuum gaps, ΔZ not necessarily corresponding to any planes or spacing of the material structure. This multi-slice formulation was originally used by Cowley and Moodie[80] as a means of obtaining the analytical N-beam solution for a parallel-sided crystal.

The phase change of the electron wave, transmitted through a thin slice, depends on the refractive index.

$$n = \left\{1 + \frac{\phi(r)}{E}\left(1 + \frac{eE}{2m_o C^2}\right)\right\}^{1/2} \approx 1 + \frac{\phi(r)}{2E} \qquad (9)$$

where $\phi(r)$, E, and m_o are potential field, the acceleration voltage and the electron mass. Then the transmission function for the plane $Z = Z_n$ representing the slice may be written in terms of a phase grating approximation

$$q_n(x,y) = \exp\{-i\sigma\phi_n(x,y) - \mu_n(x,y)\} \qquad (10)$$

where μ_n is the absorption function.

Fourier transforming

$$\begin{aligned} Q_n(u,v) &= \mathcal{F}\{q_n(x,y)\} \\ &= \mathcal{F}\{\exp[-\mu_n(x,y)] \cos \sigma \phi_n(x,y)\} \\ &\quad - i\mathcal{F}\{\exp[-\mu_n(x,y)] \sin \sigma \phi_n(x,y)\} \end{aligned} \tag{11}$$

where $\sigma = \pi/\lambda E$. λ and E are the wae length of the electrons and the acceleration vollage respectively. The validity of weak phase object approximation (WPOA)[81] with an absorption potential peaked at the atom position even in the case of a strong phase object when an objective aperture is placed in the back focal plane of objective lens, was discussed by Fejes.[82] The total effect of a crystal on an incident wave is then given by repeating (n-1) times of the unit process which converts a wave leaving the $(n-1)^{th}$ slice to the wave leaving the n^{th} slice, namely,

$$\psi_n(u,v) = \{\psi_{n-1}(u,v)\ P_{n-1}(u,v)\} * Q_n(u,v) \tag{12}$$

where $P_n(u,v)$ is the propagation function used for transfer of the wave from one slice to another and is given, in reciprocal space, by

$$P_n(u,v) = \exp\{\pi i \lambda \Delta Z(u^2+v^2)\} \tag{13}$$

For periodic object,

$$\psi_n(h,k) = \Sigma_{h'}\ \Sigma_{k'} \psi_{n-1}(h',k')P_{n-1}(h',k')Q_n(h-h',\ k-k') \tag{14}$$

The process of multiplication and addition of a set of numbers, represented by the above equation, can be done by a computer. Then, starting from a known incident wave $\psi_o(u,v)$, repetition of thisprocess gives the diffracted amplitudes after transmission through any number of slices. The real space amplitude, $\psi_n(x,y)$, at the exit surface is obtained by summing the Fourier series with $\psi_n(h,k)$ as coefficients and from this, the in-focus microscope image can be obtained. The out of focus images are given by multiplying the $\psi_n(h,k)$ by the appropriate propagation function transform values $P_R(h,k)$. The effect of lens aberrations is simulated by adding a phase shift depending on higher orders of h/a and k/b. Error is introduced in the multislice method by having to take finite slices, but this can be reduced to any arbitrary size by reducing the slice thickness at the cost of computer time.

The present program, "ZOLZ PROG" used in this study, does not allow the crystal structure to be varied in the direction of the electron beam and makes a projection approximation or "Zero Order Laue Zone approximation." It consists of three subprograms, FCO 128, Defract 128 and Image 128 which must be run in succession to obtain a simulated lattice image. Briefly, FCO 128 calculates the Fourier coefficients of the crystal potential for the nearest electron beam direction. Atom coordinates may be supplied referred to any choice 'A' of unit cell; the program will find a new primitive cell 'B' whose 'C'axis is near the electron beam direction. The beam direction IR is given with respect to cell 'A', the program prints out all the Miller indices for

the old cell 'A' and the transferred indices referred to cell 'B'. Defract 128 performs the multiple electron scattering calculations (equivalent to solving the time-independent Schrodinger equation) by the Cowley-Moodie multislice method,[80] while Image 128 synthesizes these beams in Fourier Series to form the electron lattice image taking into account all instrumental aberrations.

The parameters that must be supplied or can be varied include atom position, the unit cell parameters, the spherical aberration coefficient (C_s), the defocus value (ΔZ), the electron wave length (λ), the beam divergence (α), the radius of objective aperture (R), the chromatic aberration coefficient (C_c), the orientation conditions and the specimen thickness.

4. EXPERIMENTAL PROCEDURE

4.1 Starting Material and Ion-Implantation

Silicon wafers, <100> oriented and p-type, having 3-10 Ωcm resistivity were obtained from a commercial supplier and cut to a proper size for ion-implantation. Prior to implantations the wafers were cleaned by a 10% HF dip followed by a deionized (D.I.) water rinse, pirahna clean, boiling in trichloroethylene and a thorough D.I. water rinse again. To ensure good thermal contact, copper specimen holders were prepared and the wafers were attached to the holders using liquid gallium metal. Gallium metal not only holds the wafers in contact, but also acts as a good heat conductor. Calculations[83] show that for typical implantation parameters such as 100 kV acceleration voltage and 1 μA beam current, the temperature of the target wafer could rise to several hundred degrees due to the deposition of the energy. For this reason, there should be a good thermal contact between the wafer and the wafer holder. No specific arrangements were made to measure the surface temperature during implantation in this experiment.

The acceleration voltage and the beam current density were kept constant at 25 kV and 1 $\mu A/cm^2$ respectively throughout the present work. Relatively low acceleration voltage was chosen so as to have a shallow implantation so that the isolated damaged regions would be within the first extinction distance for high resolution imaging. The beam current was kept constant during all implantations in order to avoid any dose rate effects in the c→α transformation. A series of

arsenic implantations was carried out with doses ranging from 10^{11} ions/cm^2 to 5 x 10^{15} ions/cm^2 at R.T. During the implantation, the wafer holder was tilted 8° to avoid channelling.

4.2 Refractive Index Measurements

The refractive index of the as-implanted layers was measured using a Gaertner Ellipsometer. The schematic diagram is given in Fig. 1. The basic principle of the technique is based upon the state of polarization with reflection of a monochromatic, collimated and polarized light. The state of polarization is defined by the phase amplitude relationships between the two component plane waves into which the electric field oscillation is resolved. One wave designated 'p' is in the plane of incidence. The other, designated 's' is normal to the plane of incidence. If the 'p' and 's' components are in phase, the resultant wave is plane-polarized. In general, reflection causes a change in the relative phases of 'p' and 's' and a change in the ratio of their amplitudes. The effect of reflection is, therefore, characterized by the angle 'Δ', defined as the change in phase and angle ψ, the arctangent of the factor by which the amplitude ratio changes. The equation[84] for the refractive index is

$$n = n_o \tan \phi_o \left[1 + \left(\frac{1-\rho}{1+\rho}\right)^2 \tan^2 \phi_o\right]^{1/2} \qquad (15)$$

where $\rho = \tan \psi \, e^{i\Delta}$ and η_o and ϕ_o are the refractive index of air and the angle of incidence respectively.

The principle of measurement of 'Δ' and ψ is explained with reference to Fig. 1. The incident monochromatic beam is transmitted in

sequence by the collimator, the polarizer and the compensator. The azimuthal orientation of these devices determine the relative amplitudes and phase difference between 'p' and 's' components of the beam. These orientations are adjusted such that the difference in phase just compensates that which results from reflection. 'Δ' is thus measured. The plane polarized reflected beam is then transmitted by the analyser to a telescope and detector. With the polarizer and compensator oriented as described, the analyser can be oriented to extinguish the reflected beam. This extinction setting measures ψ. This technique was used to determine the refractive indicies of the implanted layers with varying doses.

4.3 Sheet Resistance Measurements

Sheet resistance is the resistance of a square independent of the dimensions of the square. It is, however, dependent on the thickness 't' and is given by $R = 1/g$, where "g" is the conductance of the square. The most common method,[85] using a linear four point probe, was applied to measure the sheet resistance of the implanted layers. This method is normally non-destructive; however the probe points may cause damage sometimes when excessive pressure is applied. The geometry of the set up is shown in Fig. 2. Current is passed through the outer two probes and the potential developed across the inner two probes is measured. For the probes resting on a semi-infinite medium, the resistivity is

$$\rho = \frac{2\pi(V/I)}{\frac{1}{S_1} + \frac{1}{S_3} - \frac{1}{S_1+S_2} - \frac{1}{S_2+S_3}} \qquad (16)$$

If the probes are equally spaced, $S_1 = S_2 = S_3 = S$ (say) and the equation reduces to

$$\rho = 2\pi S\ (V/I)\ \Omega\text{-cm} \quad . \tag{17}$$

More often, a large enough sample to be considered infinite is not available and in those cases, the above equation is not directly applicable. However, since the four point probe offers the most convenient mode of resistance measurement, a variety of correction factors have been developed.[85,86] They are summarized in Appendix (1).

The measurement procedure consists of:

(a) determination of the reproducibility of the resistivity measurement

(b) determination of probe spacing

(c) determination of the accuracy of the voltmeter and ammeter.

4.4 TEM Specimen Preparation and Geometry

The geometry and preparation method were exactly followed as described in Reference (87). The wafers, after ion-implantation, were cut to 3 mm discs using an ultrasonic cutting tool. These discs were mounted on a teflon sheet upside down and the entire back side was covered with parafin wax except a small center portion. This teflon sheet together with the 3 mm disc was dipped into a freshly prepared (1:2::A:B) of previously prepared solution 'A', containing 2.5 gms Iodine in 1100 CC CH_3COOH, and solution 'B', containing 1:3::HF:HNO_3. Too much stirring or agitation of the solution was

avoided in order to prevent breaking of thin regions of the specimen. Just prior to the formation of a perforation at the center, the Silicon wafer transmits red light when a bright light is placed below the beaker containing the etching solution. This indicates that the region is thin enough to expect the formation of a hole at any time. As soon as a small hole appeared at the center, the sample was taken out of the beaker and thoroughly rinsed with D.I. water. The specimen was removed from the wax and cleaned using boiling trichloroethylene (TCE) and acetone. Final rinse was done with ethanol.

This procedure gives a wedge-shaped geometry as shown in Fig. 3. The thickness of the specimen, in the areas of interest, is extremely critical for high resolution imaging and image interpretation. The influence of thickness on the contrast and spacing of lattice fringes has been discussed by Hashimoto.[77] Intensity profiles and the spacing of fringes vary with the thickness of the crystal and the deviation from the Bragg angle. The optimum thickness would be 1/4 (Extinction Distance) and that is the reason for choosing shallow implantation. A very common problem, that was encountered during specimen preparation and its subsequent handling, was loss of the ultra-thin regions of interest becasue the Silicon is mechanically brittle. Extensive care had to be taken throughout to mininize this serious problem.

4.5 High Resolution TEM: Microscope Conditions and Operation

The basic principles of high resolution imaging and the problems associated with the techniques as well as interpretation have been described in several articles.[77,88-93] The image contrast is due to

the phase difference induced in the electron wave after interaction with the specimen. This is in contrast with the more conventional techniques such as bright field (BF) and dark field (DF) imaging where the contrast is chiefly derived from amplitude variations of the electron wave after interaction with the specimen. In the former case, it is called "phase contrast imaging" and latter case, "amplitude contrast imaging." Another difference stems from the fact that the image is formed by recombination and interference of more than one beam under stringent conditions of focus. This is achieved by placing a suitable aperture in the back focal plane of the objective lens. The importance of including as many beams as possible for the formation of the image is very well illustrated in Ref. (78).

A Siemens Elmiskop 102, operating at 100 kV and having a point to point resolution ~3 Å, was extensively used for the present investigation. The microscope was equipped with a specially-designed objective lens with spherical aberration coefficient c_s ~1.2 mm and chromatic aberration coefficient $c_c \approx 1.6$ mm for high resolution imaging. By lowering the specimen holder deeper into the objective lens, one can get higher lens excitation which facilitates much lower values of c_s. The microscope also has the facilities of ±45° double axis tilting, specimen height control and a LaB_6 filament for higher brightness. The filament tip was placed 480 μm below the bias shield aperture plane in order to optimize source intensity. This requires some restrictions on the quality of the vacuum, but in general, pressure should be $<10^{-5}$ torr. This vacuum level can be achieved without

any elaborate modifications. LaB_6 filaments, which are most extensively used in modern microscopes, may be less desirable than the pointed tungsten filaments for high resolution applications due to some remaining discrepancies over the energy spread of current generation.

Careful attention was given throughout this work to the alignment of the microscope. Optimum alignment can be achieved when the magnetic field of the objective lens is rotationally symmetric, the electron beam is aligned parallel to this current axis and the center of the object plane is imaged onto the center of the image plane. Acceleration voltage was kept at 100 kV. The filament was operated in a slightly undersaturated condition in order to ensure coherency. If the filament is operated in the undersaturated condition, the energy spread of the beam can be decreased by the reduction of excess thermal energy.

4.5.1 Orientation

The specimens were tilted in such a way as to excite a systematic row of (111) type diffracted spots. A very common problem, that was encountered while tilting the specimen, was to lose the areas of interest from the field of view. A more rapid method was to observe the image under dirty dark field (DDF) condition, choosing the diffracted spot of interest by slightly displacing the aperture and tilting the specimen until the areas of interest were strongly illuminated. Another way is to follow the "road map" of Kikuchi bands and image the regions near the <110> pole. This method may not always be successful.

4.5.2 Astigmatism Correction

Once the proper orientation is obtained, all that one has to do is to place the objective aperture that includes the number of beams selected for imaging and increase the magnification to about 500000 X, while correcting the astigmatism of the objective lens. This looks very simple and straightforward, giving a false impression that HREM can be accomplished with little effort. However, the most tedious and time consuming part of the microscopy is correcting the astigmatism. Astigmatism can be regarded as an extreme form of coma; it occurs for very oblique beams when a bundle can not be considered as even approximately passing through a point. Instead, it forms a tapering wedge shaped pencil, the edge of the wedge forming what is known as a focal line. All the beams pass through this line and then diverge. But, the taper continues to cause the rays to pass through another focal line perpendicular to the first. The consequence of this defect is that it is impossible to produce a focused image of the outer parts of a plane object perpendicular to the axis.

Astigmatism is reflected in the form of asymmetry of diffractogram halos of an amorphous specimen or amorphous-like regions near the edge of the foil. This is one of the lens aberrations which is under the operators control for correction. Usually, it is corrected, in-situ, by the standard Fresnel fringe method, described in Ref. (94), but a more precise way is to use the optical diffractogram technique.

4.5.3 Focusing

Exact focusing conditions do not produce easily interpretable images in the HREM as the spherical aberration coefficient, c_s, introduces additional phase distortion given by

$$\chi(u) = \frac{2\pi}{\lambda} c_s \frac{\lambda^4 u^4}{4} + \Delta Z \frac{\lambda^2 u^2}{2} \qquad (18)$$

In order to compensate for the effect of c_s, the objective lens should be underfocused making ΔZ in the above equation negative. The optimum defocus value, defined by Scherzer,[74] is given by

$$\Delta Z_{sch} = 1.2 (c_s \lambda)^{1/2} \qquad (19)$$

This can easily be achieved during the operation of the microscope from the minimum contrast condition. At this minimum contrast condition, which occurs for the flattest configuration of the transfer function ($\sin \chi = 0.3$), $\Delta Z_{min \cdot cont} = 0.44 (c_s \lambda)^{1/2}$. This is easily observable and, therefore, serves as a reference point from which the operator can quantitatively adjust the focus and reach the Scherzer defocus condition from the known c_s and λ values. All that is required is to quickly calculate the difference between ΔZ_{scher} and $\Delta Z_{min.cont}$ and change the objective lens excitation accordingly. Once the Scherzer defocusing condition was established, the images were recorded in through focus series from -220 Å to 220 Å from the ΔZ_{sch} value as a precautionary measure. This procedure not only ensures proper focusing conditions but also saves excessive use of photographic film.

4.6 High Resolution Image Analysis

4.6.1 Optical Microdiffraction

The optical microdiffraction is a very convenient and powerful technique for the analysis of high resolution images.[95,96]. It is an extension of a commonly employed technique "optical diffraction," which has become a routine exercise in HREM in recent times. The basic principles and the application of optical diffraction were described by several investigators[97-99]. Using a He-Ne laser light to illuminate the HREM micrograph of an amorphous specimen or the edge of a TEM foil which invariably looks amorphous and acts as an optical grating, the range of spatial frequencies recorded during HREM imaging and hence the transfer characteristics of the objective lens can be precisely determined. Form the optical diffraction of the micrographs, usually referred to as "optical diffractogram," the methods to determine the contrast transfer function (CTF) and almost all the importantimaging parameters such as defocus, astigmatism, spherical aberration, drift, spatial and temporal coherene and the voltage and current centers with respect to the electron optic axis are discussed in detail in Ref. (100).

4.6.2 Periodic Extension Method

A novel method was developed to obtain diffraction information from the damage clusters of size as small as ~20 Å diameter.[101] Although the basic principle is similar to optical microdiffraction utilizing a field limiting aperture in the optical bench as described in Ref. (95), this method was designed to overcome the difficulties in the conventional technique. In conventional microdiffraction, the

diffraction effects from the sampling aperture itself often interfere with the interpretation of the results. This problem becomes more serious when diffraction information from the amorphous regions is required. This new method is based upon a periodic extension of small regions in two dimensions from which a microdiffraction pattern is desired. By using a periodic array of the segments from the damage clusters reproduced as a photographic negative, the optical diffractograms can be obtained. A preliminary attempt is made to usethis methd for the characterization of the isolated amorphous zones. See the Appendix IV for details.

4.6.3 Optical Simulation

The basic idea is to determine the point defect concentration at which the long range order will be lost and the material will appear to be amorphous. For this, two dimensional models of Silicon lattice in <110> projection with known and deliberately introduced vacancies and <110> split self interstitials were prepared as shown in Fig. 16. The defect concentration was varied from 5 to 20%. Relaxation effects were neglected to avoid complexity. Photographic negatives were carefully prepared with ~25 times reduction in size. These negatives were placed in the ray path of He-Ne laser beam, at normal incidence, which produced Fraunhofer diffraction patterns related to the spatial frequencies present in the original model patterns. These were recorded on a conventional photographic film, exactly under identical conditions, for all the models with varying point defect concentration. Care was taken to avoid diffraction effects from the aperture.

5. EXPERIMENTAL RESULTS

High resolution electron microscopy (HREM), coupled with other techniques such as optical refractive index and electrical sheet resistance measurements, was successfully applied to study the crystalline-to-amorphous transformation (c→α) in arsenic-implanted Silicon. Individual damage regions of size <45Å diameter were identified with high precision as described in the following.

5.1 Refractive Index and Sheet Resistance Measurements

The as-implanted wafers with varying doses were subjected to optical refractive index (n) and electrical sheet resistance measurements using an ellipsometer and linear four point probe set-up. The results are shown in Fig. 4. It may be noticed that the sheet resistance is insensitive to the dose until the critical dose is reached and rapidly increases at a dose of $\sim 5\times10^{14}$ ions/cm^2. On the other hand, the optical refractive index vs. log D plot shows two regions marked I and II with slopes 0.1 and 0.53 respectively below the threshold dose, in agreement with the results of Baranova et al.[34] The other interesting points noteworthy in the results are (i) both the refractive index and electrical sheet resistance show a decrease in value for specimens with doses greater than the critical dose and (ii) the refractive index measurements show the peak at a much smaller value of the dose (5×10^{13} ions/cm^2). These measurements were initially carried out to determine the critical dose (ϕ^*) for the c→α transformation at room temperature. Determination of critical dose helps to identify the

proper dose regimes for high resolution microscopy and eliminates some of the unnecessary trial-and-error work.

5.2 High Resolution TEM

Figure 5 is a conventional TEM image of heavily damaged <100> Si implanted with 100 KeV arsenic at a dose of 1×10^{14} ions/cm^2. Co-existence of crystalline and amorphous regions can be seen from this TEM image. The electron diffraction pattern consists of spots characteristic of crystalline material and Debye-Scherrer rings characteristic of amorphous regions. The image does not give much information on the character of the damage regions and c/α interface, thus necessitating the use of HREM for detailed understanding of the c→α transformation at the atomic level.

Figure 6 is a HREM image of Si <110> with a dose of 1×10^{12} ions/cm^2. This was taken at a magnification of 3×10^5x on the EM negative and defocus value $\Delta Z \approx -880$Å. The calculated value of ΔZ_{scher} is -800Å for the Siemens Elmiskop 102 used in this study at an operating voltage of 100 kV. The {111} lattice planes with a spacing of 3.1Å were clearly resolved. A small amorphous or damage cluster of diameter ~12Å at the core of an edge dislocation can be noticed in Fig. 6. The presence of the dislocation can be realized by counting the fringes on the left as well as the right side of the damage cluster. Region "A" in the figure is the edge of the foil which always gives amorphous-like mottled structure due to contamination in the microscope at the thin regions.

Another specimen with an implantation dose of 1×10^{13} ions/cm^2 was observed in high resolution mode and the image is shown in Fig. 7. This image was taken at an electron-optical magnification of 4×10^5x using a defocus value of -880Å and subsequently magnified by 10x. The defocus value is close to Scherzer defocus condition. The damage regions marked A, B, and C in Fig. 7 are of size ~50Å diameter and are spaced ~100 Å apart in the crystalline matrix. Figure 8 is the magnified image of region 'A' in Fig. 7 giving more detailed nature of the damage region and the c/α interface. The interface is only of the order of few lattice spacings with a typical width of ~12Å. The core of the region A has a typical mottled structure characteristic of amorphous specimen.

The images of another specimen with a critical dose of 5×10^{13} ions/cm^2 (Fig. 9a and 9b) show interesting features. These two images were taken from different parts of the same specimen. Figure 9a shows a small crystalline island surrounded by an amorphous material. The size of the crystallite is quite small and the presence of {111} type cross fringes can be distinctly seen from the optical diffractogram shown in the insert. The spots correspond to {111} planes in the Silicon lattice. At the places where the interface is seen edge-on, the fringes characteristic of crystalline material end abruptly and the c/α interface looks to be very sharp and smooth at atomic level. But in another region of the specimen, the lattice fringes are highly distorted and broken (Fig. 9b) and co-existence of crystalline, highly damaged and amorphous regions (marked CR, DR and AR) can be noticed. The boundaries between these regions are not

distinct, but it is clear that even the crystalline regions (CR), there are some packets or islands of amorphous regions inter-mixed with the crystallites.

A similar result was obtained in the case of specimen implanted with arsenic at a dose of 1×10^{13} ions/cm^2 but at liquid nitrogen temperature (77°K) as shown in Fig. 10. Co-existence of amorphous and crystalline regions may be noticed in Fig. 10. The lattice fringes of the crystalline regions are broken and distorted indicating that these regions are damaged, containing high defect concentration, but still possessing crystallinity. These features seem to be the same in the specimens implanted near the critical dose; but there is a subtle difference between room temperature and liquid nitrogen temperature implantations. The degree of crystallinity in the crystalline packets is more pronounced in the case of room temperature implantation. This might be due to agglomeration or clustering of points defects created during the implantation temperature. Whereas, in the case of liquid nitrogen temperature implants, the wafer is never heated up above room temperature and hence, the defect clusters are perhaps smaller and more numerous.

5.3 Lattice Image Simulations

Experimentally, it was observed that the crystalline and amorphous phases co-exist with clearly-resolved interfaces, the sharpness of the interface being influenced by its orientation with respect to the electron beam direction. The periodic structure characteristic of the crystalline material almost always ends abruptly at the interface and a mottled structure characteristic of the amorphous material on the other

side of the interface is noticed. This at first seems unlikely as there could be a gradient in concentration of point defects across the c/α interface. It is therefore expected that the lattice fringes should gradually disappear and the mottled strucure should eventually emerge giving rise to a diffuse interface in contrast to the experimental observation. It is therefore speculated that the actual concentration of point defects has some role in influencing the visibility of lattice fringes. There could be a critical concentration of point defects at which the lattice structure no longer shows a regular periodicity. In order to support this argument theoretical analysis of the lattice fringe images was done with varying point defect concentration. The results of the computer simulations are shown in Fig. (11 to 15). Atomic models of the silicon lattice in <110> projections, as discussed in Chapter 4 with varying point defect concentration, were constructed and a fully-dynamical multi-slicecomputation scheme was used for lattice fringe image simulations. The unit cell consisted of 890 atoms at a thickness of 3.84Å which is the interplanar spacing of {110} planes. The simulations were done for three different crystal thicknesses (10, 20, and 30 slices) under three different focusing conditions (-440Å, -660Å and -880Å). The simulations incorporated all the microscope parameters characteristic of the Siemens Elmiskop 102 (E_o = 100 kV, C_s = 1.2 mm and C_c = 1.6 mm).

Figure 11 is the output of Def. 128 program showing the potential distribution in the unit cells, considered in the present simulations, in the electron beam direction. Figure 11a, b, and c are for 5%, 10%, and 15% defect concentrations respectively. It is quite clear that Fig. 11 resembles the atomic models shown in Fig. 16. Presence of vacancies and split <110> self-interstitials can easily be noticed in Fig. 11. The simulated lattice fringe images of {111} planes are shown in Figs. 12-15 for a perfect lattice with no defects (Fig. 12) and a lattice containing defect density of 5% (Fig. 13), 10% (Fig. 14) and 15% (Fig. 15) for varying crystal thicknesses at three different defocus values. The scattering calculations in the multi-slice program incorporate 2580 beams and the crystal is tilted in such a way that only one reflection (111) is strongly excited. An objective aperture of radius of curvature 0.19 $Å^{-1}$ includes both the transmitted beam and Bragg reflected beam (111 type reflection) for the image formation.

It can be seen in Fig. 12 to 15 that with the increase of point defect concentration from 0 to 15%, there is a gradual change in the image from perfect fringes to less and less distinct fringes. This feature is more distinct in Fig. 13a, 14a, and 15a with a crystal thickness of ~40Å. At higher thickesses, on the other hand, this feature is less distinct, possibly because of absorption-induced dynamical effects.

5.4 Optical Simulations

The same two dimensional models of a Silicon lattice in <110> projection containing a defect density of (a) 0%, (c) 5%, (e) 10%, (g) 15%, and (i) 20% were again used on the optical bench, in the form of

photographic negatives, to get the Fraunhofer diffraction patterns. The results are shown in Fig. 16. It is clear from Fig. 16 that with the increase of point defect concentration from 0% to 20% (Fig. 16a to 16i), the spot pattern, characteristic of a periodic object, gradually becomes less and less distinct and the amorphous halos, characteristic of an aperiodic object become more distinct. The significance of these results will be further discussed in the next chapter.

5.5 1.2 MeV Electron Irradiation

A thin foil of <110> Silicon (p-type) was exposed to a high energy electron beam for about 20 minutes at 1.2 MeV in the high voltage microscope at room temperature (R.T.). The objective of this experiment was to see the effect of high energy electrons on inducing 'homogeneous' nucleation and growth of amorphous clusters in unimplanted Silicon. The actual specimen temperature during irradiation could have been above R.T., but it was not measured. The electron beam was focused to a size of ~2μm on the specimen maintaining a beam current density of 5×10^{-9} Amps/cm^2. No electrical charge accumulation was found during the irradiation process. This could be due to the low current density used for this study. The total electron dose was estimated to be 4×10^{13} electrons/cm^2. The energy of these electrons is high enough to displace the atoms in the Silicon lattice from their regular sites, thus producing vacancies and interstitials.

After irradiation, the specimen was transferred to the Siemens 102 for high resolution imaging of the irradiated regions. Figure 17a is the conventional bright field (BF) image of the irradiated area of the specimen at low magnification. The region, encircled, is further

magnified and shown in Fig. 17b. The most striking feature of Fig. 17b is that it shows what may be clustering of interstitials generated during the irradiation (Regions marked P, Q and R).

The same regions (P, Q and R) were imaged in high resolution mode to further characterize the nature of their structure. Fig. 17c,d, and e show lattice images of these regions with the {111} type planes clearly resolved. The size of these regions is of the order of 25-30Å. In Fig. 18, the high resolution image of the region 'P' is shown under different defocus conditions ranging from -660Å to -1320Å. It can be noticed from Fig. 18a-d that the contrast of the region 'P' decreases relative to the matrix as the defocus value changes from (a) to (d).

To verify the possibility of contamination within the microscope, the lattice fringe images were simulated with a cluster of interstitials deliberately introduced in the atomic model as shown in Fig. 19 using the previously described fully-dynamical-multislice program under tilted illumination conditions. The simulated images support the possibility of obtaining darker contrast due to interstitial clusters as suspected. The implications of these results will be further discussed in Chapter 6.

6. DISCUSSION

There has long been speculation as to how the nucleation of an amorphous phase takes place in radiation-damaged crystalline materials. There are two phenomenological models available for the crystalline-to-amorphous transformation in Silicon, in particular as discussed in Chapter 2, applicable respectively to light and heavy ions. Moreover, the term 'heterogeneous nucleation' which is widely used in the literature is somewhat misleading. It is true that near the end of the range of a heavy ion, there could be enough localized displacement damage for the formation of an amorphous zone, but this is not a heterogeneous nucleation event in the classical sense. The mechanism of the c→α transformation and the nature of the damage that leads to the formation of amorphous zones still is not well understood.

An attempt is made in the present investigation to study the c→α transformation in arsenic-implanted Silicon at room temperature using High Resolution Electron Microscopy (HREM). A few general comments need to be mentioned before proceeding further. All the high resolution images presented here show a typically mottled structure characteristic of an amorphous material at the edge of the foil. This indeed is quite a common observartion in all high resolution microscopy work irrespective of the nature of the specimen. It is a general belief[78] that this feature is probably due to contamination and therefore should not be confused with the ion-implantation damage regions. Improper imaging conditions can also lead to a mottled image structure which might be confused with a damage crystal image. Extreme caution is

therefore needed to be sure to avoid this effect. However, the observation of many regularly-spaced isolated damage regions (e.g. A, B, C of Fig. 6) in the present study rules out this possibility. It is very unlikely that the observed zones were due to any artefact. The model proposed below is based upon the belief that these are the radiation induced amorphous zones.

6.1 Unified Model of the c→α Transformation

6.1.1 Nucleation of Amorphous Zones

As stated by Titov[103], every projectile ion in an implantation process produces a plasmoid of vacancies and interstitials, which during their short life time, either agglomerate to clusters, mutually annihilate or seggregate at other defect clusters or sinks. The probability that a particular event will dominate depends on various factors such as the mobility of individual point defects, temperature, interaction of various defects and so on. If the temperature is high enough for the mobility of individual point defects but not for defect clusters, it is anticipated that nucleation of the amorphous phase will take place by agglomeration of point defects or by migration to existing defect clusters, foreign atoms, dislocations or grain boundaries (a true heterogeneous nucleation). The stress field of some existing defects is strongly attractive for the elementary point defects. As shown in Fig. 6, a dislocation core may have acted as a nucleation site for the formation of an amorphous zone.

Though the ion implantation process is performed nominally at room temperature, the actual temperature of the specimen could be 50-100°C higher and in this temperature range, elementary point defects are

known to be mobile while divacancies, trivacancies and larger clusters of vacancies and interstitials are not. The elementary point defects, therefore, quickly migrate to the sinks such as larger clusters of point defects and dislocation lines. In the present case (Fig. 6) such a phenomenon may have occurred at a dislocation line leading to a classical heterogeneous nucleation of the amorphous phase.

With increase of ion dose, more isolated amorhous zones, ~50 Å in size were found to be nucleated. No dislocations were usually found; however, the nucletion sites could have been small dislocation loops formed by clustering of interstitials. It is not likely that these isolated amorphous regions A, B, and C in Fig. 7 were created by individual implanted ions at the end of their trajectories. The flux was too high to correlate with such a small number of relatively large amorphous zones.

Whether the nucleation takes place directly at the heavily damaged zone near the end of an ion track or not should depend not only on the type of ion (light or heavy) but also on the temperature. If the temperature is low enough to prevent long range migration of defect clusters but high enough for the mobility of individual point defects, the nucleation can be heterogeneous in the sense that amorphous zones form at already damaged material in the vicinity of a small interstitial cluster even for light ion damage such as boron. At low temperatures with low mobility of individual point defects, the nucleating defect cluster may be more often associated with the end of an individual ion track particularly for the case of a heavy ion. The lattice may relax

suddenly to an amorphous state at these regions when the concentration of the point defects locally reaches a critical value.

A true homogeneous nucleation involving a homogeneous distribution of mobile point defects and nucleation of amorphous phase homogeneously in the matrix when the defect concentration reaches a critical value as suggested by Chadderton[72] might take place if the temperature is high enough for a uniform distribution of generated point defects and there are no heterogeneous sites such as dislocations. This seems highly unlikely. Such a phase transition is extremely difficult to verify experimentally. Probably a direct observation during electron irradiation of a perfect crystal might help. It is the competetion between the rate of generation and rate of migration of the point defects that determines the temperature at which the nucleation mechanism would change from heterogeneous type to homogeneous type. At still higher temperature coarsening of interstitial dislocation loops occurs so that the total dislocation density can never reach high levels.

A point that has never been clear so far is whether or not a damaged zone that contains more than some critical concentration of point defects undergoes relaxation to a lower energy amorphous state which is in some way distinctly different from a crystal containing a high density of point defects. If such a relaxation does occur, there should be sharp interfaces in partially amorphous material separating the regions that have relaxed from those that have not. In Fig. 6, an amorphous zone is seen in the vicinity of a dislocation core. The

observations in Fig. 6, Fig. 9 and Fig. 10 are consistent with the hypothesis that a sufficiently damaged crystal does relax to an amorphous phase at some critical point defect concentration. Figures 9a,b show a small crystalline island surrounded by an amorphous material and co-existence of crystalline and amorphous phases intermixed together with sharp interfaces. At the places where the interface is seen edge-on, the lattce fringes characterstic of crystalline material end abruptly; in a distance of the order of an atomic dimension the image changes from distinct fringes to the mottled image characteristic of an amorphous material.

The simulated lattice fringe images in Figs. 12-15 show that such a sudden disappearance of lattice fringes would not be expected unless there is an abrupt change in the structure. It is clear from the results that for a gradual increase in point defect concentration, there is a corresponding gradual change in the image from perfect fringes to less and less distinct fringes. At 15 percent Frenkel pair concentration, the image is close to that characteristic of an amorphous material, but the change is very gradual. Incidentally, this value without incorporating local lattice relaxation, agrees well with the estimated value of 10% by Christel et al.[33] In order to experimentally verify the fraction of atoms to be displaced before the crystalline material relaxes to an amorphous state, a systematic study was conducted using the optical diffraction technique as described in Chapter 4.6.3. Figure 16 show that as the Frenkel pair concentration increases from 0 to 15%, the spot pattern characteristic of a periodic object gradually becomes less and less distinct and the amorphous halos

characteristic of an aperiodic object become clearer. This result is in agreement with the results of image simulations and the argument that the amorphous state does not appear to be reached simply by increasing the point defect concentration until lattice order gradually disappears. The position of the boundary of the amorphous zones presumably corresponds to the surface inside of which the critical concentration of point defects necessary for the damaged crystal-to-amorphous transformation has been reached.

6.1.2 Growth of Amorphous Zones

Growth of the amorphous volume and finally the formation of a 100% amorphous layer with the increase of ion dose can take place by two mechanisms: (a) by the growth of the existing amorphous zones and (b) nucleation of increasing number of amorphous zones and their overlap. In a crystalline matrix, these small zones should only be metastable so long as the point defect concentration in the surrounding crystal stays below the critical level. They should shrink by a net transfer of atoms across the interface from the amorphous side to the crystalline side. However, the migration of an amorphous-crystalline interface needs an activation energy >2.4 eV.[104,105] At room temperature, the thermally activated rate of migration would be negligible. Simultaneously with the formation of amorphous zones, however, interstitials and vacancies which are mobile at R.T. will be created in the crystalline material. All the previously formed crystalline amorphous interfaces should act as sinks for these defects. Their recombination at the interface and other radiation-induced transfer of energy to atoms at the

interface should provide the necessary activation energy for a continuous partly athermal shrinkage of all existing amorphous zones. Therefore whether a 100% amorphous layer would be formed or not formed would depend upon the relative rates of formation of new amorphous zones and shrinkage of existing ones.

According to this model,[106] at liquid nitrogen temperature (LNT) where self interstitials and vacancies are immobile, the shrinkage rate will be negligible and the point defect concentration in the crystalline regions should also increase to the critical level at which existing amorphous zones might expand. At the other extreme (high temperatures) the point defect concentration, except near the ends of the ion track will never reach the critical value and amporphous zones might shrink faster than new zones are created. A continuous amorphous layer would, therefore, never be formed.

As the temperature increases, the kind of damage that builds up in the crystal changes. At low temperatures, the damage is expected to be rather homogeneous consisting of elementary point defects; their mobility is restricted. Therefore, the nucleated amorphous zones may arise from elementary point defects distributed randomly. Near room temperature elementary point defects are no longer frozen in place, they tend to cluster and hence the smallest stable defects would be divacancies and larger clusters of vacancies and interstitials. With increasing temperature, it is expected that the spectrum of defect complexes distributed randomly in the matrix will shift to larger and larger clusters until a temperature is reached when dislocation loops of interstitial type predominate. Therefore, the amorphous material formed

at higher temperature is expected to be less homogeneous. This could explain the differet regrowth behavior of amorphous layers formed at low and high temperatures by ion implanation.[102]

The behavior in both the electrical sheet resistance and optical refractive index measurements can also be explained in the general context of the above model. For example, region I in the refractive index vs. log (D) plot corresponds to a low dose regime with a relatively slow increase in n. In this dose range, it is not ureasonable to consider two simultaneous processes that are independently occurring: (a) direct formation or nucleation of new amorphous regions whose number increases relatively slowly with the increase of dose and (b) a gradual accumulation of point defects and their clusters in the crystalline but damaged regions. In region II, the sudden change in the refractive index might be due to the fact that with the continuous accumulation of point defects in the crystalline damaged region, a sudden nucleation of many more amorphous zones might be occurring, thus rapidly increasing the total fraction of amorphous material.

6.2 High Energy Electron Irradiation

In order to study the effect of high energy electrons on inducing nucleation and growth of amorphous clusters in an unimplanted Silicon, a thin foil of <110> Si was irradiated with 1.2 MeV electron beam near R.T. In Fig. 17b it can be seen that there is an uniform distribution of defect clusters giving black and white contrast. The high resolution images of these clusters (e.g., P, Q, and R) indicate that they are of the size 25-30Å. The depth distribution is hard to predict from these images. A similar effect of irradiation in Silicon was

reported by Thomas[107] after 20 minutes of irradiation at 700 kV at R.T. and by Foll[108] after irradiation with 650 kV electrons at low temperatures giving a similar black and white contrast.

Frenkel pairs created by the electron beam at these dose levels either recombine spontaneously, migrate to surface sinks or participate in the clustering process depending upon how far the interstitials and vacancies are separated from each other and from the sinks. Near room temperature, presumably, the mobility of vacancies is much higher than that of interstitials and therefore those interstitials which are far away from vacancies may cluster or be trapped at existig defects such as impurities.

Assuming that each electron produces a Frenkel pair, the steady state concentration of Frenkel pairs produced during irradiation at an electron flux (ϕ) of ~3.3×10^{10} electrons/cm^2/sec used in the present study is estimated to be ~$6 \times 10^{15}/cm^3$/sec. From this, the saturated cluster density is calculated using the method of Makin[109] and found to be ~$2.37 \times 10^{14}/cm^3$. The experimentally observed cluster density is ~$2 \times 10^{12}/cm^3$ assuming a crystal thickness of 500Å. With the error involved in determining the cluster density and the error in the thickness value assumed, it is reasonable to think that both the theoretical calculation and the experimental observation are in agreement. Therefore, it is tentatively believed that such a clustering process is occurring in the present case leading to a darker contrast in the regions of the clusters. Further systematic experiments need to be carried out to confirm this.

The possibility that the dark contrast zones could be due to contamination was studied by two independent methods: (a) examining the high resolution images of the same area under different defocus conditions (Fig. 18). A thin layer of contamination is expected to give rise to Fresnel fringes at the edges with defocusing, (b) lattice fring image simulation (Fig. 19) with a cluster of interstitials. The simulation did show a region of darker contrast. Small clusters like this may eventually evolve into amorphous zones.

SUMMARY AND CONCLUSIONS

In spite of many past experimental as well as theoretical investigations, the production of disorder and the mechanism of the crystalline-to-amorphous (c→a) transformation in tetrahedrally-bonded semiconductors such as Si and Ge have yet to be completly understood. The main points of debate include (i) whether the nucleation of an amorphous phase is indeed 'homogeneous' or 'heterogeneous' in character in the classical sense, (ii) whether a heavily damaged region relaxes to an amorphous state when the point defect concentration reaches a critical value, (iii) whether the c/α interface is smooth or rough at atomic level and (iv) how the nucleated amorphous zones grow for complete amorphization. An attempt is made in the present investigation to understand this fundamental phase transformation in arsenic implanted Silicon using high resolution electron microscopy. The following conclusions can be drawn.

1. Whether the nucleation is 'homogeneous' or 'heterogeneous' should not only depend on the mass of the ion implanted but also on the temperature. From the present observations, it seems unlikely that there is any case where nucleation of amorphous zones takes place in a truly homogeneous way.
2. If the temperature is low enough to prevent long range migration of small defect clusters but high enough for the motion of elementary point defects, nucleation of an amorphous phase is likely to take place by formation of a localized high density region of small clusters.

3. A crystalline region containing a high enough point defect or cluster concentration does appear to relax to an amorphous state. In partially damaged crystal, isolated amorphous and crystalline regions do co-exist with sharp interfaces. Lattice image simulations support this conclusion.
4. Growth of the amorphous zones and the transition to complete amorphization depend upon the temperature which effects the mobility of the point defects, dose rate and the mass of the implanted ion. It is the competition between the rate of generation and rate of thermal and athermal annealing of amorphous zones that determines whether the amorphous zones grow or shrink. This needs further study.
5. High energy electron irradiation experiments gave evidence for clustering of interstitials near room temperature.

ACKNOWLEDGMENTS

The author would like to express his sincere acknowledgments, with pleasure, to Dr. Ronald Gronsky and Professor Jack Washburn for their invaluable guidence, inspiration and stimulating discussions with active interest during the entire part of this research, to Prof. Nathen Cheung for his helpful discussions and patience to review this thesis, to Mr. Roar Kilaas for his great help on computer simulations and brotherly working companionship and to Mr. David Ackland, Mr. A. Gronsky and other technical staff on the electron microscope for their constant help throughout. Deep appreciation is extended to the technical staff of 432 Cory Hall, Department of Electrical Engineering and Computer Sciences for providing ion-implantation facilities. Last but not least, the author would like to extend his sincere thanks to Ms. Valerie Kelly and Mrs. Sharon Kerst for typing the thesis. Laboratory facilities and financial support were provided by the U.S. Department of Energy through the Materials and Molecular Research Division of Lawrence Berkeley Laboratory.

The author is highly obligated to his daughter, Radhika, wife, Vijaya Lakshmi and parents-in-law who constantly motivated and provided strong moral support since the beginning of this research.

Appendix I

LINEAR FOUR-POINT-PROBE FORMULAS AND CORRECTION FACTORS

Configuration	Comments
1. Thick sample, boundaries > 10S from probes	No corrections required, $\rho = 2\pi S(V/I)$
2. Thick sample, near edge	For non-conducting boundaries the error may be as high as 100%
3. Circular rod	Applicable to pulled crystals
4. Thin sample, with $W < 0.1S$ and boundaries >20S from probes	$\rho = 4.53\ W(V/I)$ $R_S = 4.53\ (V/I)$

APPENDIX II

RECOVERY OF POINT DEFECTS IN SILICON[110]

	Defect Type	Silicon Doping (n or p)	Activation Energy (eV)	Annealing Temp (°K)
1.	Double negatively charged monovacancy	n	0.18	70-80
2.	Single negatively charged self interstitial	n	0.30	130-140
3.	Electrically neutral monovacancy	p	0.33	150-180
4.	Singly positively charged orthorhombic <110> split self interstitial	p	0.85	370-420
5.	Electrically neutral tetragonal <100> split self interstitial	p and intrinsic	0.92	540-600
6.	Divacancy	n and p	1.5	570-670

APPENDIX - III

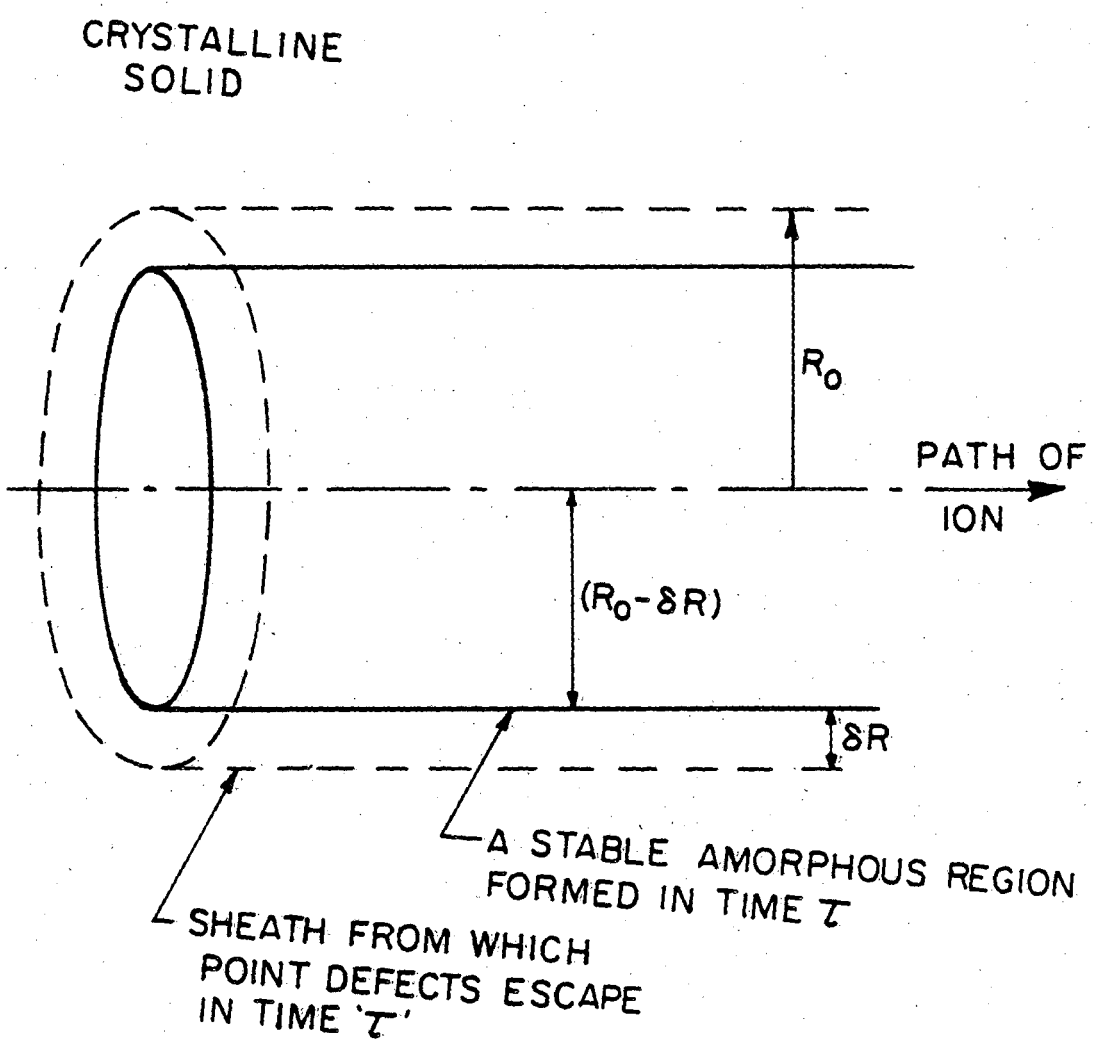

XBL829-6530

APPENDIX IV

There is no known direct method to precisely characterize the structure of amorphous zones of size <50Å (e.g., amorphous zone in Fig. Ia). In the conventional optical microdiffraction method using a small (0.5 mm dia) selected area aperture, the diffraction effects from the aperture often interfere with those from the amorphous zones causing a serious problem for interpretation. This is evident from the Fig (Ib). A new method based upon periodic extension of the amorphous zone as a two dimensional array Fig. Ic) was developed to overcome this problem. The success of this method is demonstrated in Fig (Id) in which tiny spots, two bright spots and amorphous halos correspond to the array, the {111} type lattice fringes and the amorphous zone respectively.

Using this method a preliminary attempt was made to distinguish the possible differences in the spatial periodicities present in various amorphous zones when the dose levels are varied. Figures (II a, b, c) are the high resolution images with varyng arsemic doses. Amorphous zones of Fig (II a, b, c) were repeated as periodic arrays as shown in Fig. (II d, e, f). Figure (II g, h,i) are the corresponding optical diffractograms. A gradual decrease in intensity and finally disappearance of {111} reflections and a gradual increase in the spatial extent of amorphous halos with increasing dose can be noticed in Fig. (II g, h, i). The spatial extent of amorphous halos in the reciprocal space is inversely proportional to the spatial periodicities in the real space. Therefore, by comparison, it could be possible to detect

subtle differences in various amorphous zones at least on a qualitative basis. More systematic experiments are needed for further use of this method.

Fig (I) Principle of 'periodic extension' method (a) same image of Fig. (7) at lower magnification (b) optical microdiffractogram of the region in square of (a) using a 0.5 mm size aperture. Diffraction effects from the aperture can be seen.

(c) Periodic array of same region but magnified by 10x.

(d) Optical diffractogram showing the diffraction from (i) the {111} lattice fringes (spots), (ii) amorphous zone (amorphous halos) and (iii) the periodic array (closely spaced spots).

Fig (II) Periodic extension applied to three amorphous zones of three specimens with varying doses (1×10^{12}, 1×10^{13} and 5×10^{13} ions/cm^2)

(a) Same as Fig. (6). (d) and (g) are the periodic array of the amorphous zone and its optical diffractogram respecively.

(b) Same as Fig. (8). (e) and (h) are the periodic array and optical diffractogram respectively.

(c) A portion of Fig. (9b). (f) and (i) are the periodic array and optical diffractogram respectively.

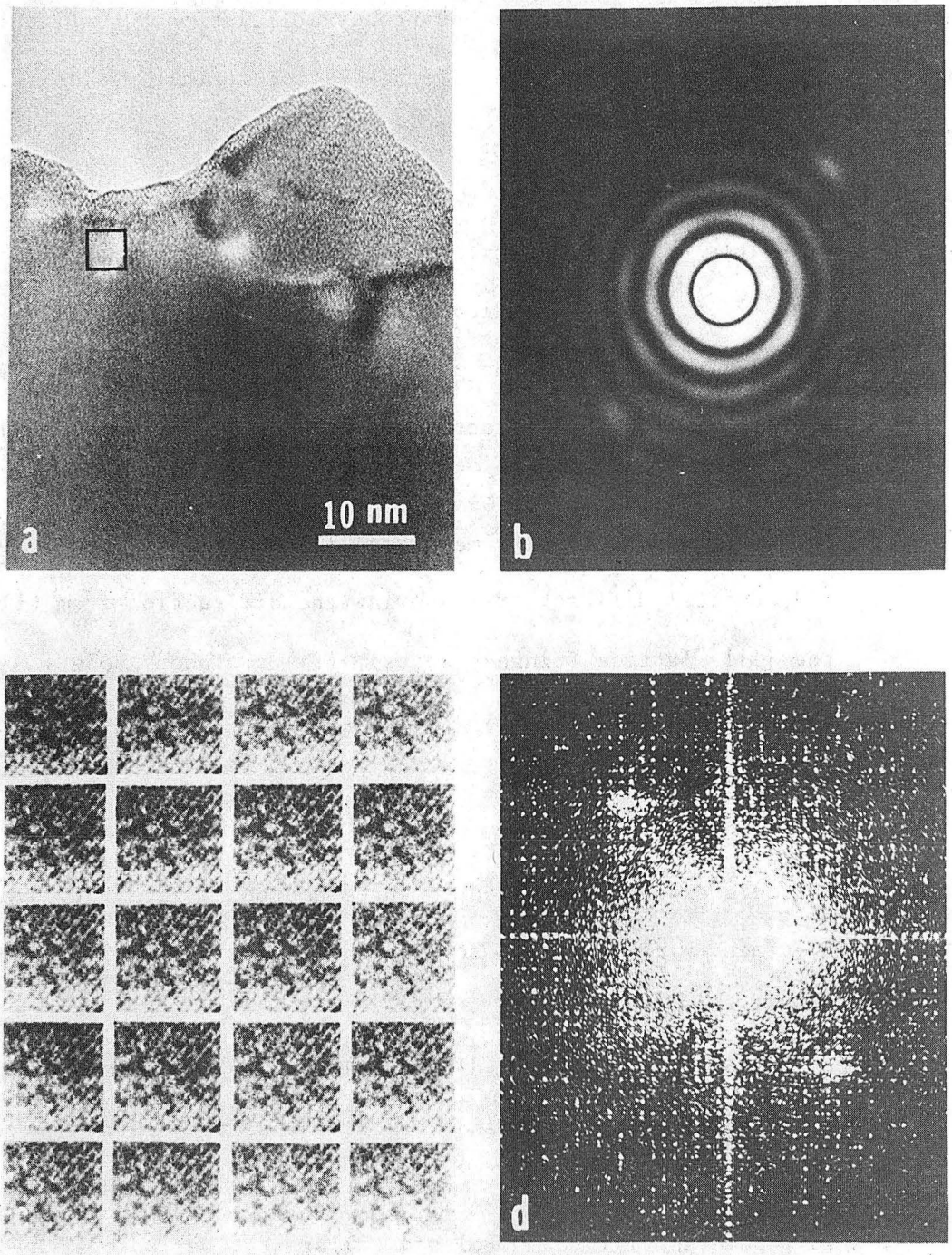

XBB 824-3370

FIGURE I

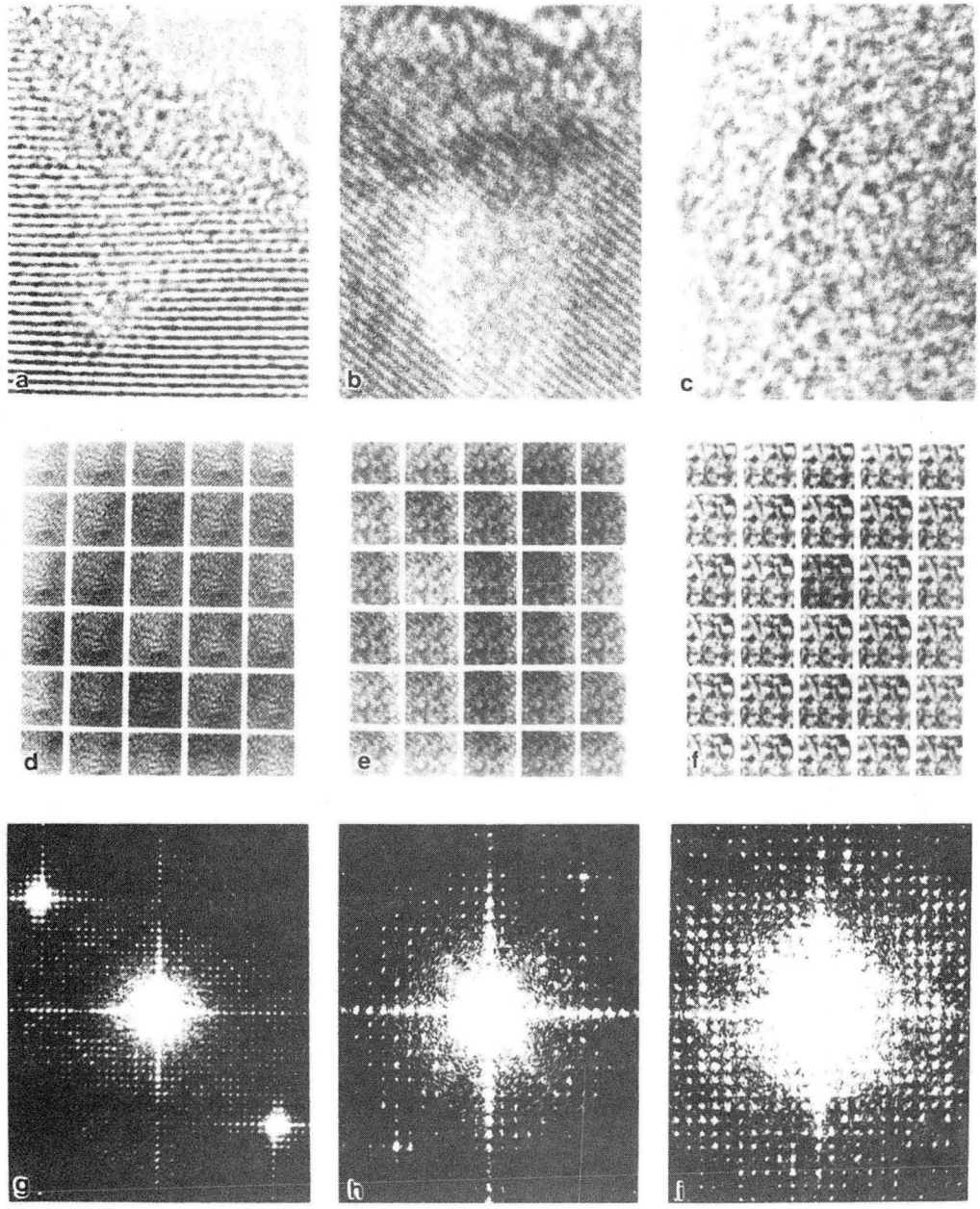

XBB 828-7162A

FIGURE 11

REFERENCES

1. J. F. Gibbons, J. L. Moll and N. I. Mayer, Nucl. Instr. and Methods 38, p. 165 (1965).
2. T. Alvager and N. J. Hansen, Rev. Sci. Instr. 33, p. 567 (1962).
3. F. M. Rourke, J. C. Scheffield and F. A. White, Rev. Sci. Instr. 32, p. 455 (1961).
4. K. E. Manchester, C. B. Sibley and G. Alton, Nucl. Instr. Methods 38, p. 169 (1965).
5. R. R. Ferber, IEEE Trans. Nuclear Science, NS-10, p. 15 (1963).
6. B. L. Crowder, "Ion implantation in semiconductors and other materials," Yorktown Heights, Plenum Press (1972).
7. B. L. Crowder, "Ion implantation in semiconductors and other materials," Osaka, Plenum Press (1974).
8. F. H. Eisen and L. T. Chadderton, "Ion implantation," Proc. 1st Int. Conf., Thousand Oaks, Gorden and Breach (1971).
9. G. Carter and W. A. Grant, "Ion implantation in semiconductors" (1976).
10. L. Amadei, R. Gereth and H. J. Queisser, J. Appl. Phys. 36, p. 1537 (1965).
11. R. Truell, Phys. Rev. 116, p. 890 (1959).
12. G. K. Wertheim, Phys. Rev. 115, p. 568 (1959).
13. (a) J. H. Crawford and J. W. Cleland, J. Appl. Phys. 31, p. 1204 (1959).

    (b) J. H. Crawford Jr., "Radiation damage in solids," Academic Press, N.Y., p. 333 (1962).

14. I. G. Salisbury and M. H. Loretto, Radiation Effects, 59, p. 59 (1981).

15. J. F. Gibbons, "Ion-implantation in semiconductors," Proc. IEEE 56, #3, p. 295 (1968).

16. P. D. Townsend, J. C. Kelly and N. E. W. Hartley, "Ion implantation, sputtering and their applications," Academic Press, N.Y., (1976).

17. G. Carter and J. S. Colligon, "Ion Bombardment of Solids," American Elsevier Publishing Company, N.Y., 1968.

18. G. H. Kinchin and R. S. Pease, Rep. Prog. Phys. 18, p. 2 (1955).

19. J. Lindhard, M. Scharff and H. Schitt, Kgl. Danske vid. Selskab, Mat. Fys. Medd, 33 (1963).

20. J. F. Gibbons, Proc. IEEE, 60, p. 1062 (1972).

21. F. Seitz and J. S. Kochler, Solid State Physics 2, Academic Press, N.Y. p. 305 (1956).

22. J. A. Brinkman, Amer. J. Phys., 24, p. 246 (1956).

23. J. A. Brinkman, "Radiation Damage in Solids," Proc. Int. School of Physics, Enrico-Fermi Academic Press, N. Y. and London, p. 830 (1962).

24. J. R. Parson and R. U. Balliffi, J. Phys. Chem. Solids, 25, p. 263 (1964).

25. A. Seeger, Proc. of Int. Conf. on Peaceful Uses of Atomic Energy, 6, N.Y., p. 250 (1958).

26. R. H. Silsbee, J. Appl. Phys. 28, p. 1246 (1957).

27. J. R. Beeler and D. G. Besco, Phys. Rev. 134 A, p. 530 (1964).

28. L. T. Chadderton and F. H. Eisen, Proc. 1st Int. Conf. on Ion Implantation, N.Y., Gordon and Breach, p. 445 (1971).

29. G. Muller and S. Kalbitzer, Phil. Mag. B., 41, No. 3, p. 307 (1980).

30. F. L. Vook and H. J. Stein, Radiation Effects, 2, p. 23 (1969).

31. H. Richter and G. Breitling, Z. Naturforsch A, 13, p. 988 (1958).

32. M. L. Swanson, J. R. Parson and C. W. Hoelke in "Radiation Effects in Semiconductors" edited by J. W. Corbett and G. D. Watkins, N.Y., Gordon and Breach, p. 359 (1971).

33. L. A. Christel, J. F. Gibbons and T. W. Sigmon, J. Appl. Phys. 52 (12), p. 7143 (1981).

34. E. C. Baranova, V. M. Gusev, Yu. V. Martynenko, C. V. Strarinin and I. B. Haibullin, Radiation Effects 18, p. 21 (1973).

35. E. T. Yen, B. J. Masters and R. Kastl in "Ion implantation in semiconductors" edited by S. Namba, N.Y., Plenum Press, p. 501 (1975).

36. M. Miyao, T. Miyazaki and T. Tokuyama, Jap. J. Appl. Phys. 17, p. 955 (1978).

37. R. C. Newman, "Infrared studies of crystal defects," London, Taylor and Francis Ltd., p. 88 (1973).

38. H. J. Stein, F. L. Vook and J. A. Borders, Appl. Phys. Lett., 16, p. 106 (1970).

39. D. A. Thompson, A. Golanski, K. H. Haugen, D. V. Stevanovic, G. Carter and C. E. Christodoulides, Radiation Effects 52, p. 69 (1980).

40. H. Kerkow, B. Lukasch and R. Pippig, Phy. Stat. Solid. (a)., 70, p. 489 (1982).

41. E. Glaser, G. Gotz, N. Sobolev and W. Wesch, Phys. Stat. Solid. (a), 69, p. 603 (1982).

42. J. W. Corbett and G. D. Watkins, Phys. Rev. Lett. 7, p. 314 (1961).

43. G. Bemski and B. Szymanski, J. Phys. Chem. Solids, 24, p. 1 (1963).

44. J. W. Corbett, "Radiation damage in Si and Ge" in Proc. 1st Int. Conf. on Ion Implantation, edited by L. Chaderton and F. Eisen, N.Y., Gordon and Breach, p. 1 (1971).

45. G. R. Booker, A. M. B. Shaw, M. J. Whelan and P. B. Hirsch, Phil. Mag. 16, p. 1185 (1967).

46. D. J. Mazey, R. S. Nelson and R. S. Barnes, Phil. Mag. 17, p. 1145 (1968).

47. S. I. Romanov and L. S. Smirnov, Radiation Effects 37, p. 121 (1978).

48. S. M. Davidson and G. R. Booker, Radiation Effects 6, p. 33 (1970).

49. B. L. Crowder, J. Electrochem. Soc., 118, p. 943 (1971).

50. R. K. Bicknell and R. M. Allen in Proc. 1st Int. Conf. on Ion Implantation, edited by L. Chadderton and F. Eisen, N.Y., 1971.

51. S. M. Davidson, "TEM studies of radiation damage in Silicon," in Proc. of European Conf. on Ion-Implantation, England (1970).

52. J. W. Mayer, L. Ericksson and J. A. Davies, "Ion implantation in semiconductors, Si and Ge," N.Y., Academic Press (1970).

53. H. J. Stein, F. L. Vook, D. K. Brice, J. A. Borders and S. T. Picraux, Proc. of 1st Int. Conf. on Ion Implantation, edited by L. Chadderton and F. Eisen, N.Y., Gordon and Breach, p. 17 (1971).

54. K. Masuda, S. Namba, K. Gamu and K. Murakami, Proc. U.S. Japan Sem. on Ion Implantation in Semiconductors, Kyoto, Japan, p. 19 (1971).

55. J. K. Hirvonen, W. L. Brown and P. M. Glotin, Proc. 2nd Int. Conf. on Ion Implantation, edited by I. Ruge and J. Graul, N.Y., Springer (1971).

56. J. E. Westmoreland, J. W. Mayer, F. H. Eisen, and B. Welch, Appl. Phys. Lett. 15, p. 308 (1969).

57. K. L. Brower and W. Beezhold, Proc. 2nd Int. Conference on Ion Implantation, edited by I. Ruge and J. Graul, N.Y., Springer (1971).

58. F. Dworschak, H. Schuster, H. Wollenberger and J. Wurm, Phys. Stat. Sol. 29, p. 75 (1968).

59. G. Della Mea, A. V. Drigo, P. Mazzoldi, G. Nardelli and R. Zannoni, Appl. Phys. Lett. 16, p. 382 (1970).

60. F. F. Morehead and B. L. Crowder, Radiation Effects, 6, p. 27 (1970).

61. F. F. Morehead, B. L. Crowder and R. S. Title, J. Appl. Phys. 43, p. 1112 (1972).

62. J. R. Dennis and E. B. Hale, Radiation Effects, 19, p. 67 (1973).

63. J. R. Dennis, G. K. Woodword and E. B. Hale, Int. Conf. on Lattice Defects in Semiconductors, Institute of Physics, London, p. 467 (1974).

64. J. F. Gibbons, Jap. Soc. Appl. Phys., August 1971.

65. J. R. Dennis and E. B. Hale, Radiation Effects, 30, p. 219 (1976).

66. J. R. Dennis and E. B. Hale, J. Appl. Phys. 49(3), p. 1119 (1978).

67. R. P. Webb and G. Carter, Radiation Effects, 59, p. 69 (1981).

68. G. Carter and R. P. Webb, Radiation Effects, 43, p. 19 (1979).

69. R. P. Webb and G. Carter, Radiation Effects, 42, p. 159 (1979).

70. G. Carter, R. P. Webb, and R. Collins, Radiation Effects, 37, p. 21 (1978).

71. F. H. Eisen and B. Welch, Radiation Effects, 7, p. 143 (1971).

72. L. T. Chadderton, Radiation Effects, 8, p. 77 (1971).

73. F. L. Vook, "Radiation Damge and Defects in Semiconductors," Institute of Physics, London, p. 60 (1972).

74. O. Scherzer, J. Appl. Phys. 20, p. 20 (1949).

75. P. B. Hirsch, A. Howie, R. B. Nicholson, D. W. Pashley and M. J. Whelan, "Electron Microscopy of Thin Crystals," Butterworths, London (1965).

76. R. D. Heidenreich, "Fundamentals of Transmission Electron Microscopy," Interscience, N.Y. (1964).

77. H. Hashimoto, M. Mannami and T. Naiki, Phil. Trans. (A), 253, p. 459 (1961).

78. R. Gronsky in "Experimental Methods of Materials Science," edited by H. Herman, Academic Press, N. Y. (1981).

79. P. Goodman and A. F. Moodie, Acta. Cryst. 30, p. 280 (1974).

80. J. M. Cowley and A. F. Moodie, Acta. Cryst. 10, p. 609 (1957).

81. J. M. Cowley and S. Iijima, Z. Naturforsch, 27a, p. 445 (1972).

82. P. L. Fejes, 30th Ann. Proc. Electron Microscopy Soc. Amer., Los Angeles, Calif., edited by C. J. Arceneaux, p. 558 (1972).

83. P. Parry, J. Vac. Sci. Tech. 13, p. 622 (1976).

84. R. M. A. Azzam and N. M. Bashava, "Ellipsometry and Polarized Light," North Holland Publishing Co., New York (1977).

85. G. Knight, "Handbook of Semiconductor Electronics," edited by L. P. Hunter, McGraw Hill Book Co., N. Y. (1956).

86. L. B. Valdes, Proc. IRE, 42, p. 420 (1979).

87. R. M. Drosd, Ph.D. Thesis, LBL #9990 (1979).

88. H. Rose, Optik 42, p. 217 (1975).

89. J. Fertig and H. Rose, Optik 54, p. 165 (1979).

90. J. C. H. Spence, 38th Ann. EMSA meeting, p. 282 (1980).

91. J. C. H. Spence, "Experimental High Resolution Electron Microscopy," O.U.P. (1980).

92. J. M. Cowley, Ann. Rev. Phys. Chem. 29, p. 251 (1978).

93. R. Sinclair and J. Dutkiewicz, J. Acta Met. 25, p. 235 (1977).

94. J. W. Edington, "Practical Electron Microscopy in Materials Science," Monograph I, Philips Technical Library, Macmillan, Eindhoven.

95. R. Gronsky, R. Sinclair and G. Thomas, 34th Proc. Electron Microscopy Soc. Am., Miami Beach, Florida, p. 494 (1976).

96. T. Tanji and H. Hashimoto, Acta Cryst. A34, p. 453 (1978).

97. F. Thon, Z. Naturforsch, 20a, p. 154 (1965).

98. S. G. Lipson and H. Lipson, "Optical Physics," Cambridge University Press, Cambridge (1981).

99. R. Gronsky, Ph.D. Thesis, LBL #5784 (1976).

100. O. L. Krivanek, Ph.D. Thesis, Trinty College, University of Cambridge (1975).

101. R. Gronsky and C. S. Murty, 40th Ann. Proc. EMSA, G. W. Bailey (ed.), Claitor's, Baton Rouge, p. 428, 1982.

102. R. Drosd and J. Washburn, J. Appl. Phys. 53, p. 397 (1982).

103. V. V. Titov, Phys. Stat. Solidii. (a) 63, p. 11 (1981).

104. L. Csepregi, J. Mager and T. Sigmon, Appl. Phys. Lett. 29, p. 92 (1976).

105. R. Drosd and J. Washburn, J. Appl. Phys. 51, p. 4106 (1980).

106. J. Washburn, C. S. Murty, D. Sadana, P. Byrne, R. Gronsky, N. Cheung and R. Kilaas, "Ion beam modification of materials" conference, France, September 1982.

107. G. Thomas, Phil. Mag., 17, p. 1097 (1968).

108. H. Foll, "Lattice Defects in Semiconductors," Institute of Physics, London, edited by F. A. Huntley, p. 233 (1974).

109. M. J. Makin, Phil. Mag., p. 1133 (1969).

110. W. Frank, "Lattice Defects in Semiconductors," Institute of Physics, London, edited by F. A. Huntley, p. 40 (1974).

FIGURE CAPTIONS

Fig (1) (a) Schematic representation of Gaertner Ellipsometer (b) and (c) showing the resolution of incident and reflected beams into 'p' and 's' component waves. Incident beam is elliptically polarized and reflected beam is plane polarized.

Fig (2) Schematic line diagram of the four-point probe set-up. S_1, S_2 and S_3 are the probe spacings and I & V are the current and voltage respectively.

Fig. (3) Schematic line diagrams of the geometry of TEM specimen
(a) orientation of Silicon wafer and As^+ implantation
(b) Silicon wafer after As^+ implantation showing the isolated damage regions
(c) Geometry of TEM specimen, after chemical thinning, showing the wedge shape.

Fig. (4) Plots of refractive index (n) and change of sheet resistance - Vs - log (dose). Dose levels were varied from 1×10^{11} to 5×10^{15} ions/cm^2. Three regions I, II, & III may be noticed.

Fig. (5) (a) Bright field (BF) image of heavily implanted <100> Silicon. Arsenic implantation dose is 1×10^{14} ions/cm^2

(b) Diffraction pattern of the corresponding region, showing Debye-Scherrer rings and spot pattern characteristic of amorphous and crystalline regions.

Fig. (6) Lattice image of <110> Si with As^+ dose of 1×10^{12} ions/cm^2 showing the {111} type planes of spacing 3.1Å and presence of a small (~12Å size) damage/amorphous region at the core of a dislocation.

Fig. (7) Lattice image of <110> Si with As^+ dose of 1×10^{13} ions/cm^2. Isolated damage regions A, B and C can be seen distinctly.

Fig. (8) Enlarged image of damage region 'A' in Fig. (7) with a clear picture of the amorphous core and the c/α interface. The c/α interface is rough at atomic level.

Fig. (9) Lattice image of <110> Si with a dose of 5×10^{13} ions/cm^2 (close to ϕ^*)

(a) Small crystalline island in amorphous matrix. Optical microdiffractogram of the crystallite is shown in the insert.

(b) Co-existance of amorphous region (AR), damaged but still crystalline region (DR) and crystalline region (CR) can be seen as marked.

Fig. (10) Lattice image of <110> Silicon with a dose of 1×10^{13} ions/cm^2 at liquid nitrogen temperature. Co-existance of crystalline and amorphous regions with sharp interfaces can be noticed.

Fig. (11) Potential distributions of the unit cells (Fig. 16 c, e, & g) considerd for image simulations. The unit cells consist of 890 atoms with Frenkel pair defect concentration of (c) 5% (e) 10% and (g) 15%.

Fig. (12) Computer simulated lattice image of {111} planes in Silicon with 0% Frenkel pair defect concentration. This image shows the success of the computer program.

FIg. (13) Computer simulated lattice images of {111} planes in Silicon containing 5% Frenkel pair defect concentration.

(a) Defocus $\Delta Z = -440$Å (b) $\Delta Z = -660$Å and (c) $\Delta Z = -880$Å for a crystal thickness of 38.4Å.

(d) $\Delta Z = -440$Å (e) $\Delta Z = -660$Å (f) $\Delta Z = -880$Å for a crystal thickness of 76.8Å.

(g) $\Delta Z = -440$Å (h) $\Delta Z = -660$Å for a crystal thickness of 115.2Å.

Fig. (14) (a) to (h) Same as Fig. (13) but with 10% Frenkel pair concentration

(i) $\Delta Z = -880$Å for a crystal thickness of 115.2Å.

Fig. (15) Same as Fig. (14) but with Frenkel pair concentration of 15%.

Fig. (16) Atomic models and optical diffractograms of various Silicon lattices in <110> projection with varying Frenkel pair concentration (a) 0% defect density, (c) 5%, (e) 10% (g) 15%, (i) 20% and (b), (d), (f), (h), (j) are the corresponding optical diffractograms. A gradual development of amorphous rings can be noticed from (b) to (j).

Fig. (17) TEM pictures of <110> Si after 1.2 MeV electron irradiation for 20 minutes at a beam current density of 5×10^9 Amps/cm^2

(a) Bright field (BF) image of area irradiated

(b) Enlarged image of the area encircled in (a). P, Q, R are the regions of interest for HREM (c), (d) and (e) are the lattice images of regions P, Q and R marked in (b)

Fig. (18) Lattice images of region 'P' in Fig (17b) under various defocus conditions

(a) $\Delta Z = -660$Å, (b) $\Delta Z = -880$Å, (c) $\Delta Z = -1110$Å and (d) $\Delta Z = -1320$Å. A decrease in contract level and lattice fringe visibility may be noticed from (a) to (d).

Fig. (19) Computer simulated lattice images of {111} planes in Silicon containing a cluster of self-interstitials

(a) Atomic model of the unit cell, considered for the simulations.

(b) Simulated lattice fringe image at the defocus value of $\Delta Z = -660$Å. The center portion has darker contrast due to the cluster of interstitials. This is consistant with the experimental observation.

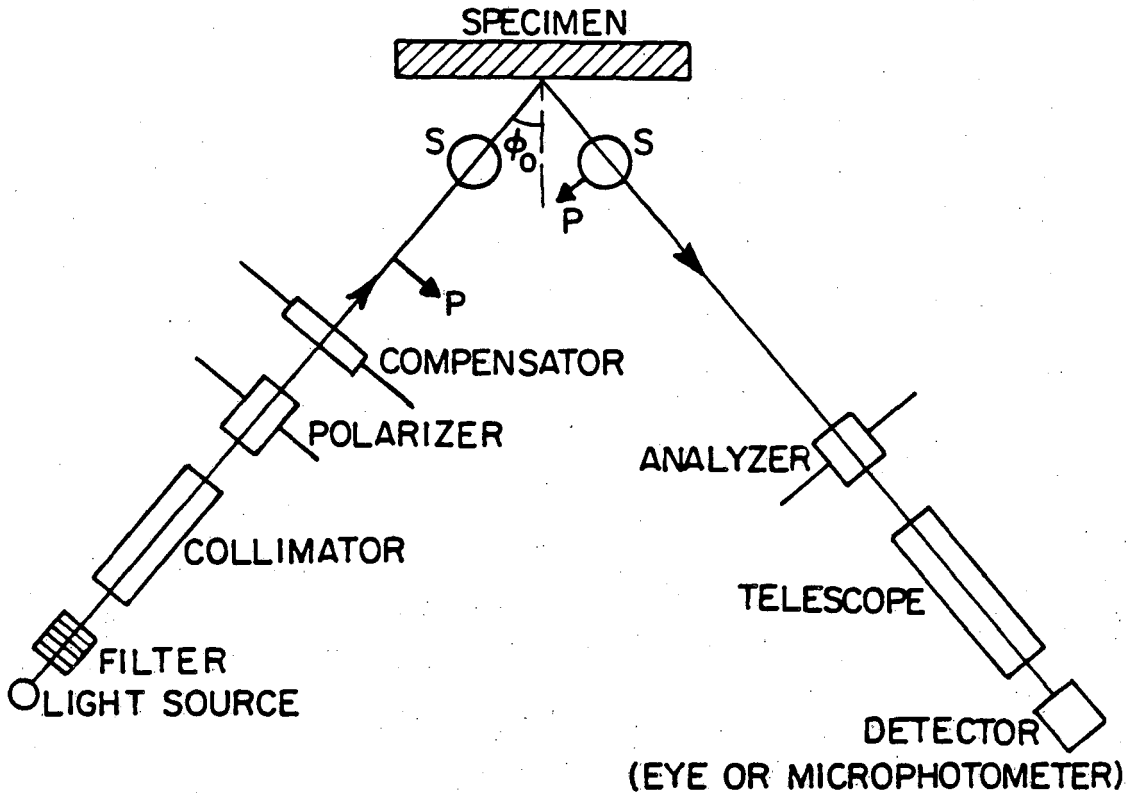
SPECIMEN
S
ϕ_0
S
P
P
COMPENSATOR
POLARIZER
ANALYZER
COLLIMATOR
TELESCOPE
FILTER
LIGHT SOURCE
DETECTOR
(EYE OR MICROPHOTOMETER)
(a)
INCIDENT
REFLECTED
S
P
TIME
(b)
S
P
S
P
(c)
XBL 829-6503

FIGURE 1

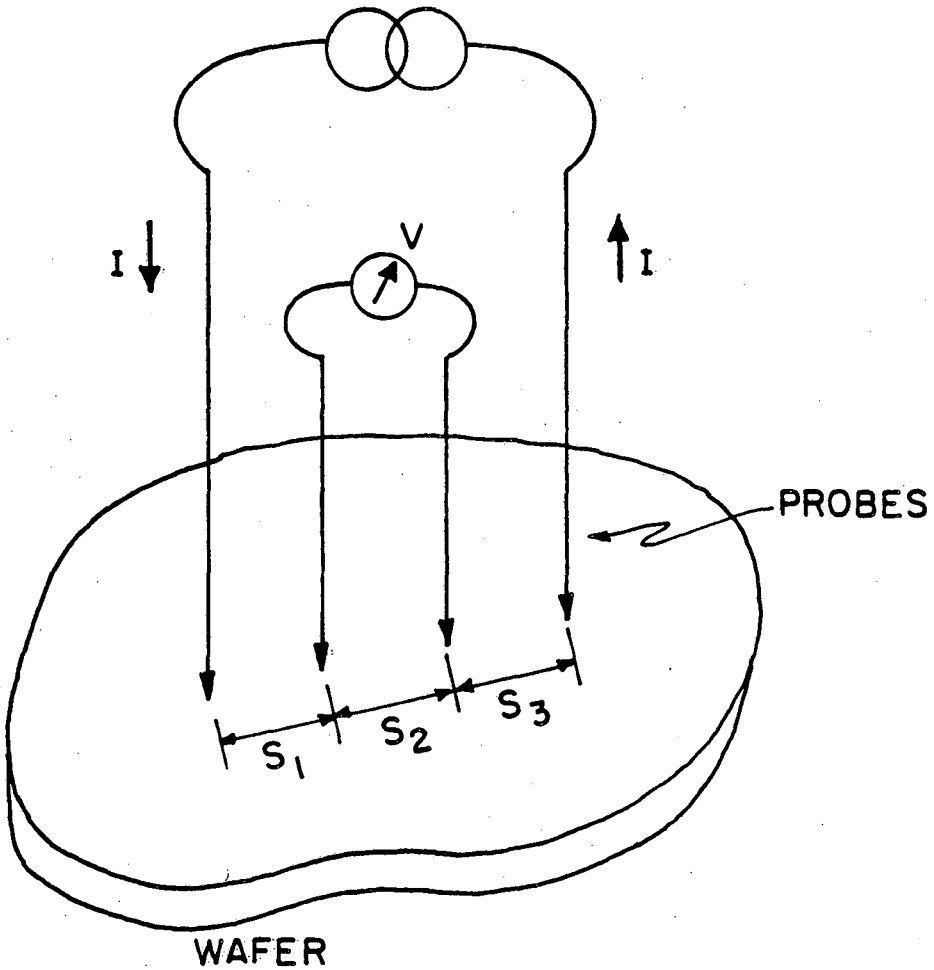

FIGURE 2

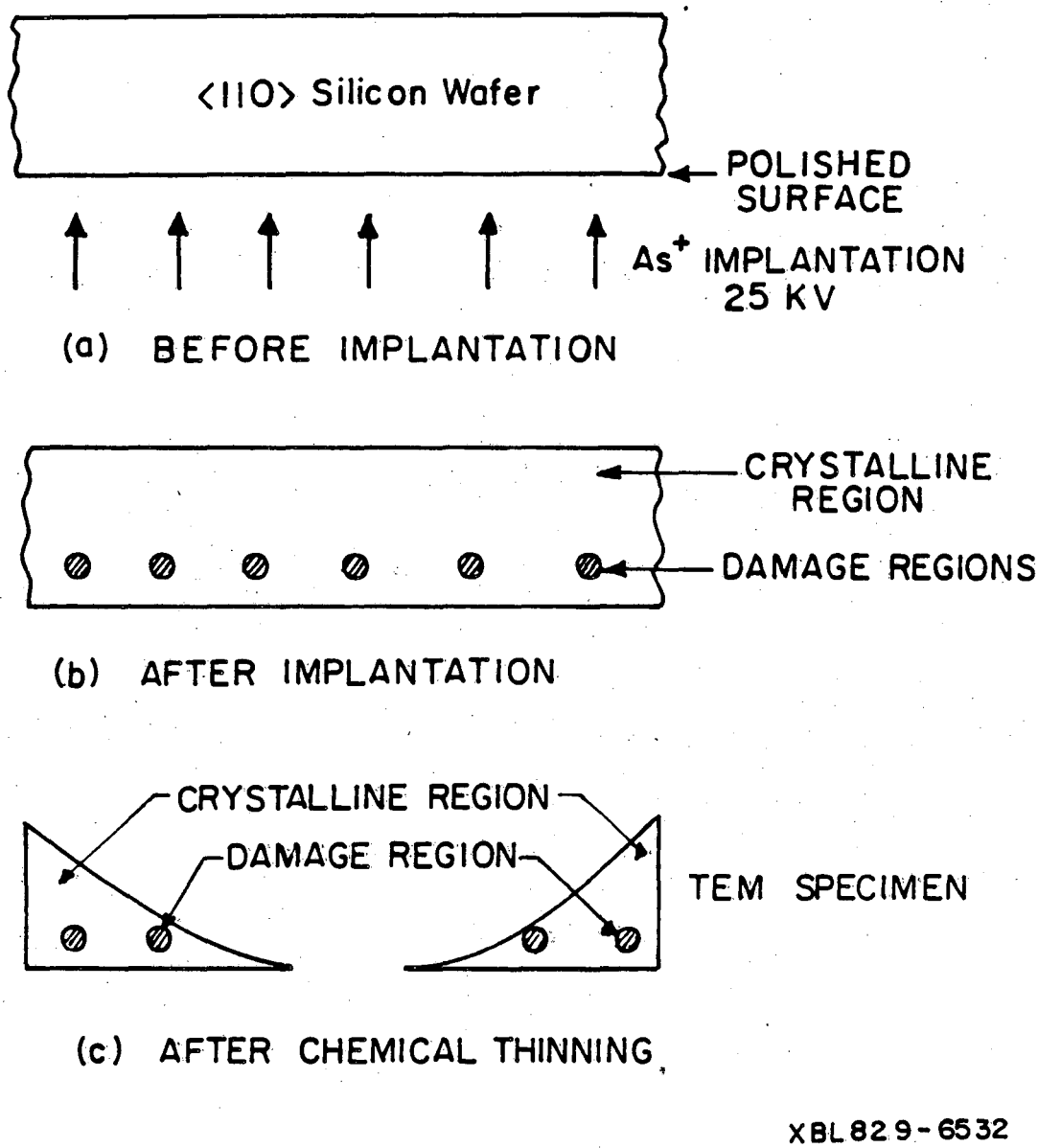
<110> Silicon Wafer
POLISHED SURFACE
As+ IMPLANTATION 25 KV
(a) BEFORE IMPLANTATION
CRYSTALLINE REGION
DAMAGE REGIONS
(b) AFTER IMPLANTATION
CRYSTALLINE REGION
DAMAGE REGION
TEM SPECIMEN
(c) AFTER CHEMICAL THINNING
XBL829-6532

FIGURE 3

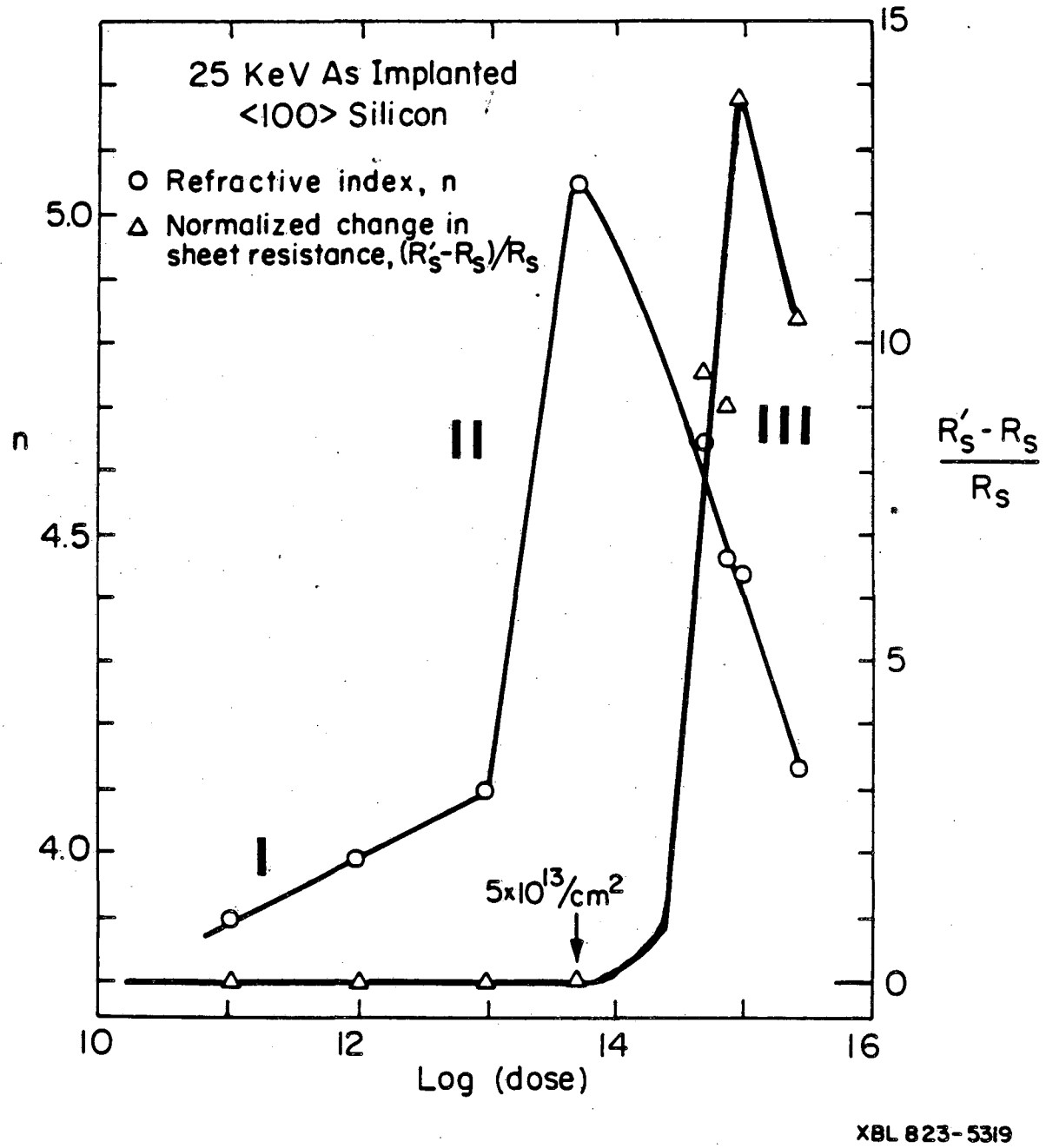
25 KeV As Implanted
<100> Silicon
O Refractive index, n
Δ Normalized change in sheet resistance, $(R_S'-R_S)/R_S$
n
$\frac{R_S'-R_S}{R_S}$
5.0
4.5
4.0
15
10
5
0
I
II
III
$5\times10^{13}/cm^2$
10
12
14
16
Log (dose)
XBL 823-5319

FIGURE 4

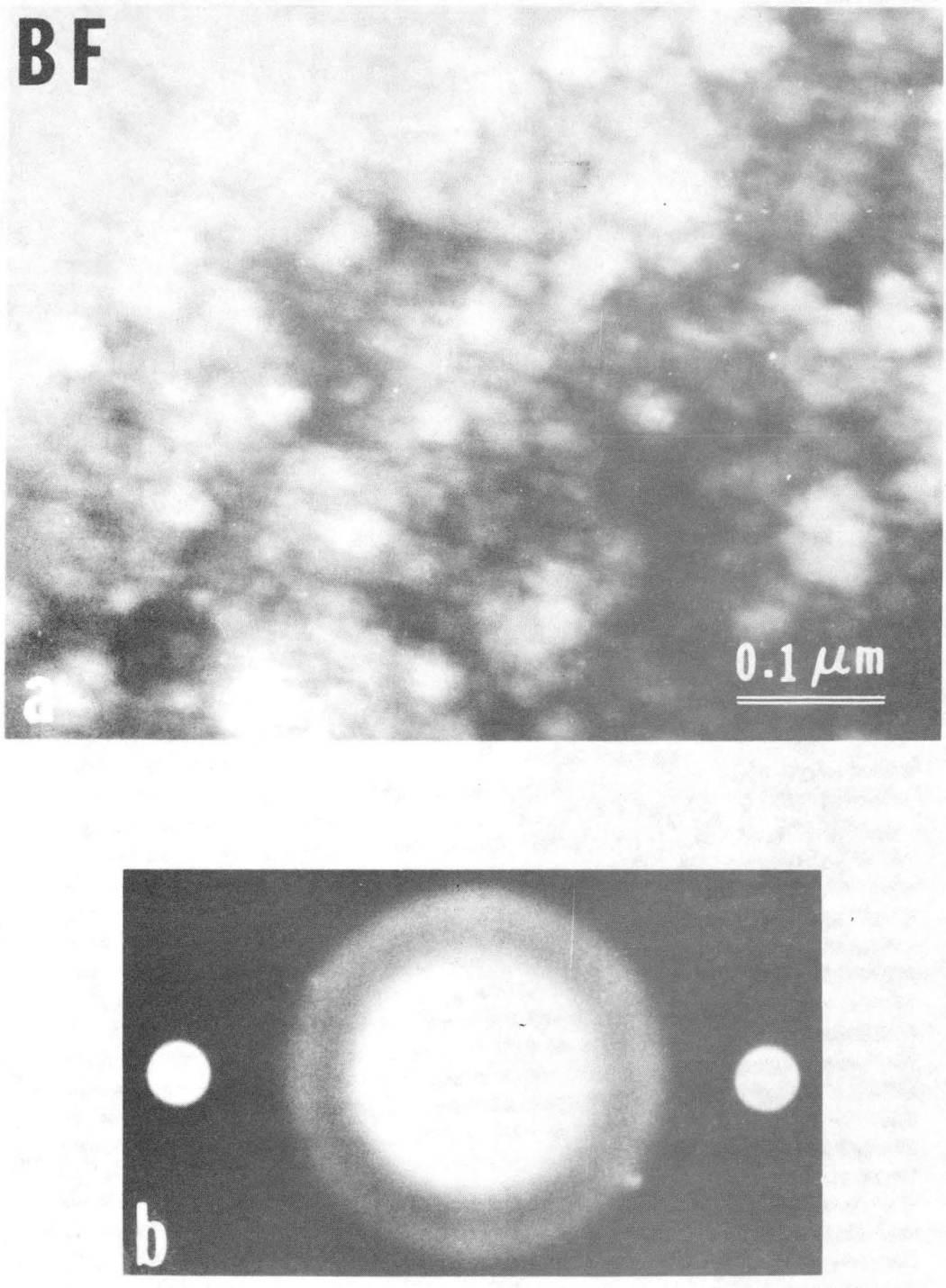

XBB 829-7686A

FIGURE 5

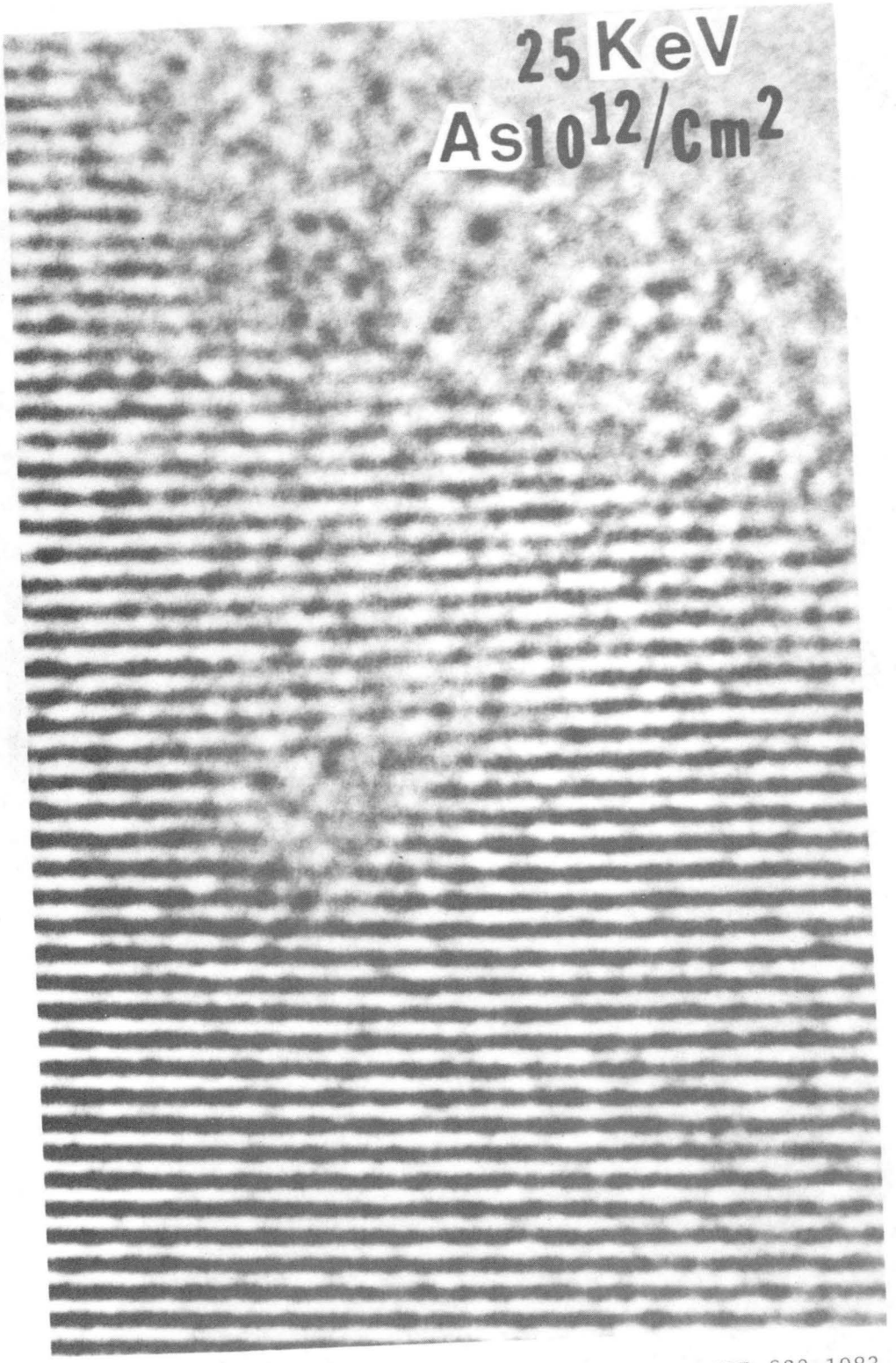

XBB 823-1983

FIGURE 6

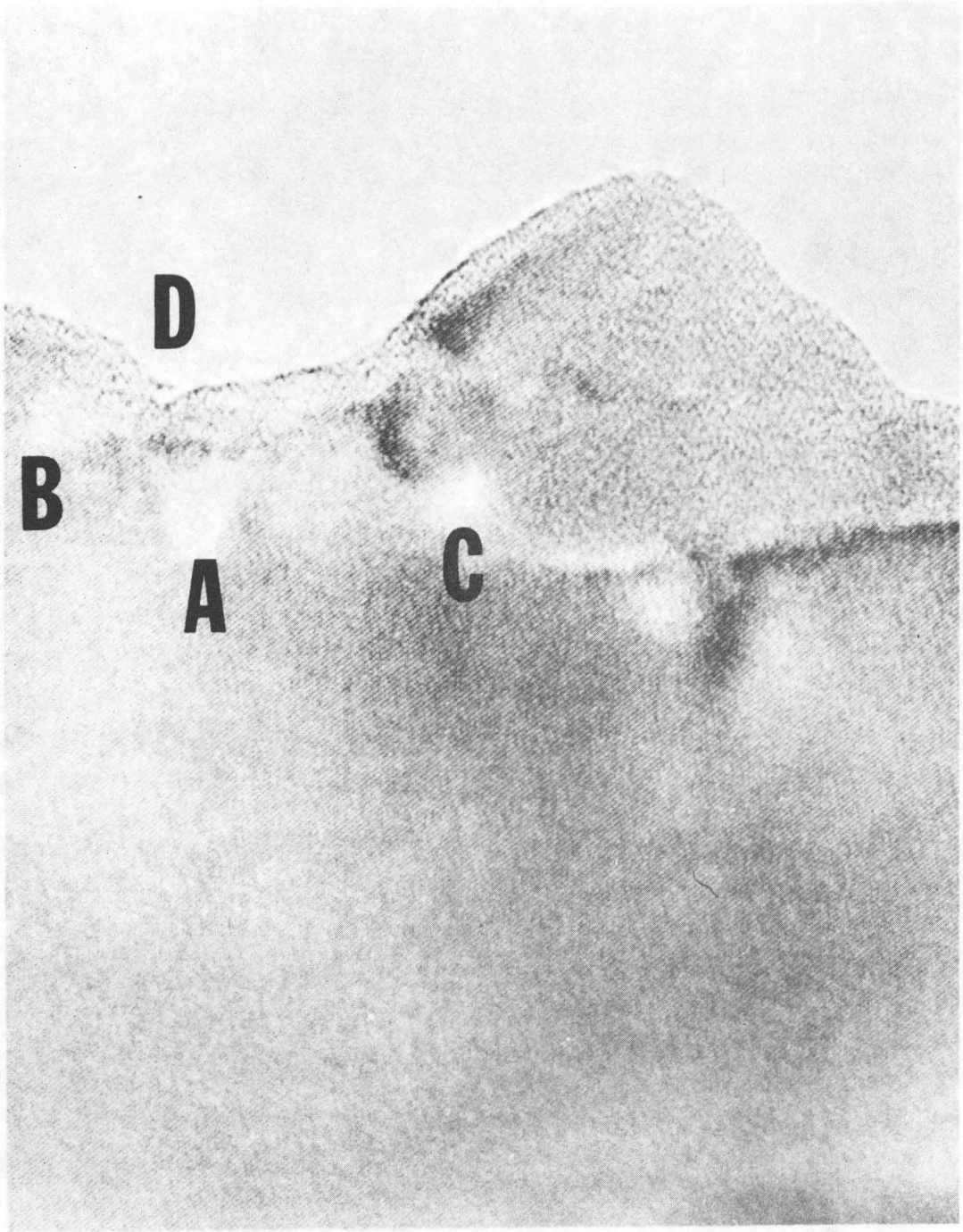

XXB 827-6077

FIGURE 7

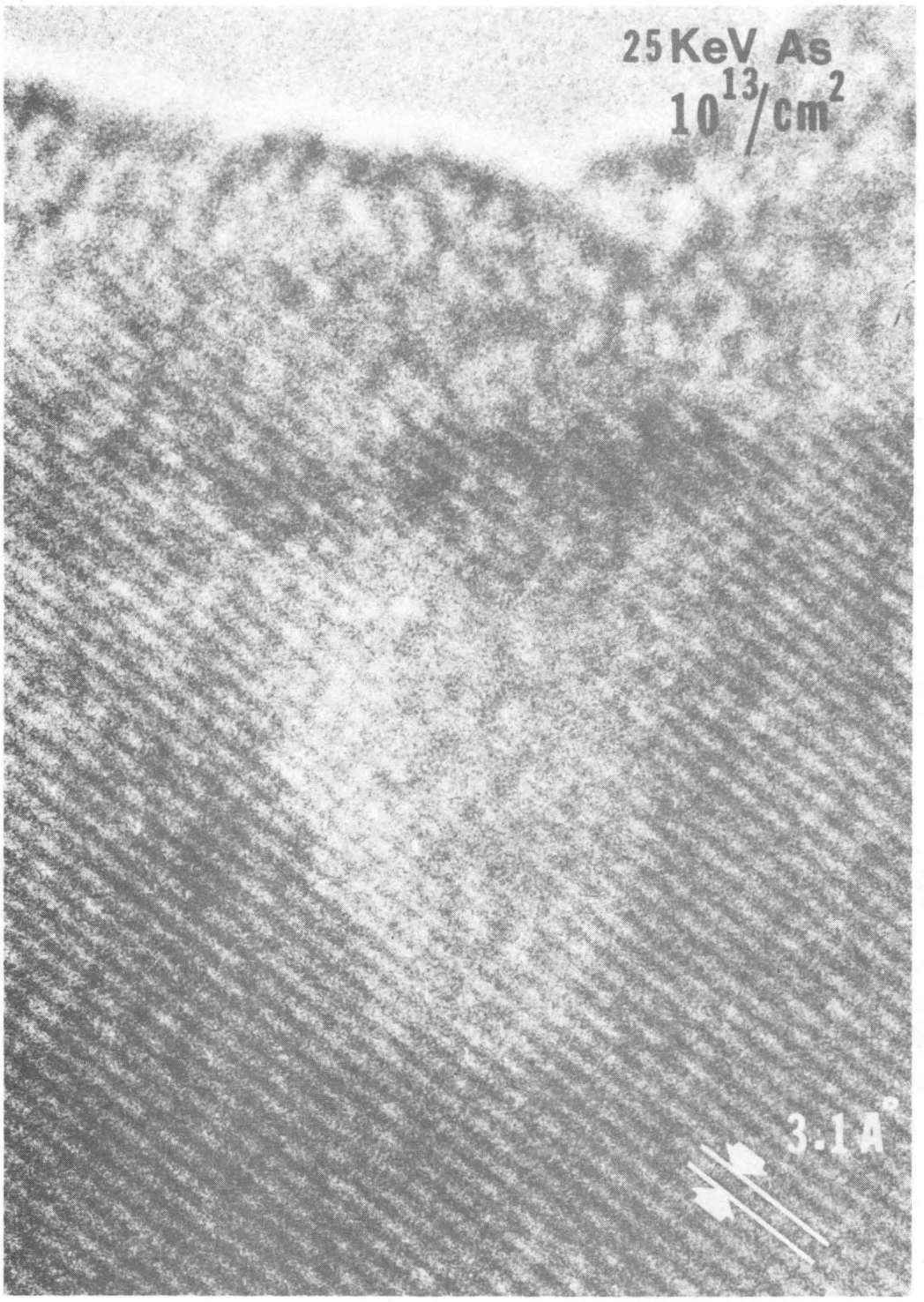

XBB 822-1457

FIGURE 8

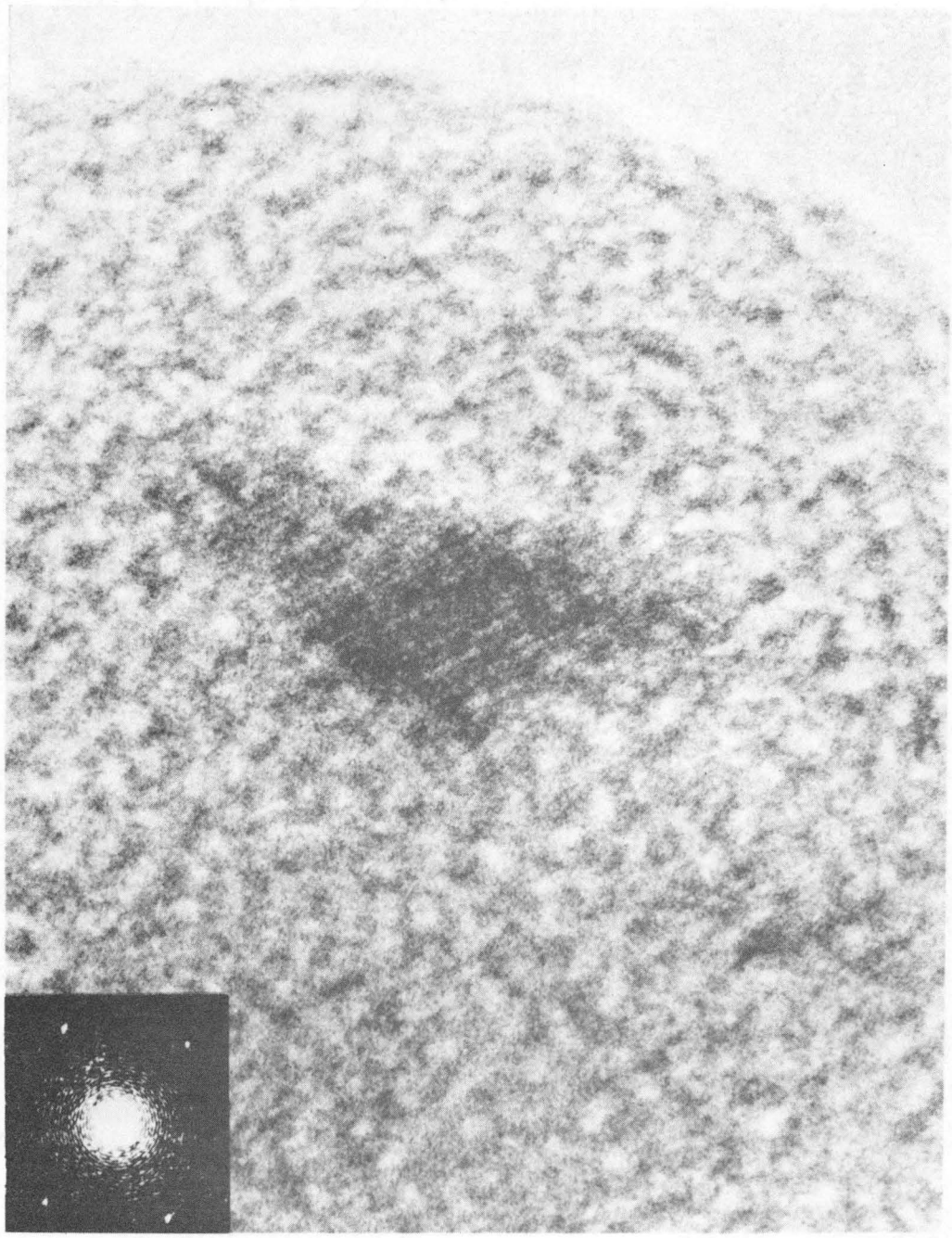

XBB 824-4056

FIGURE 9a

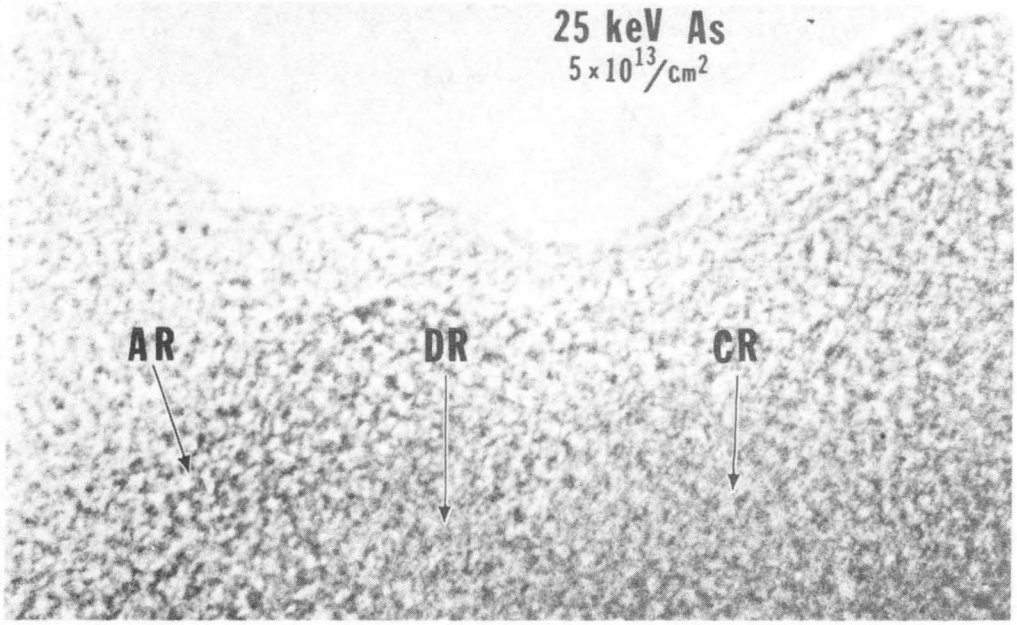

XBB 820-8793

FIGURE 9b

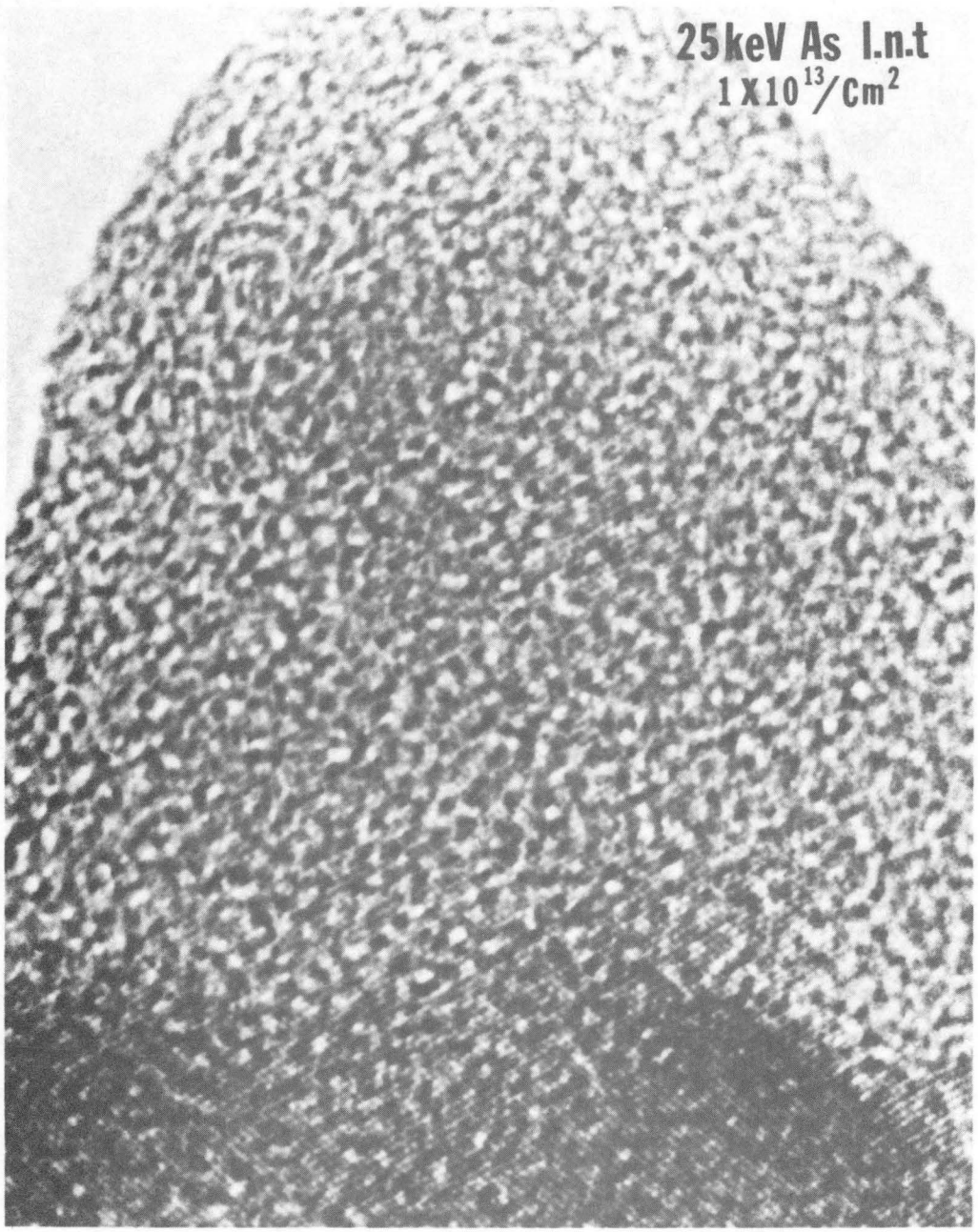

XBB 824-3334

FIGURE 10

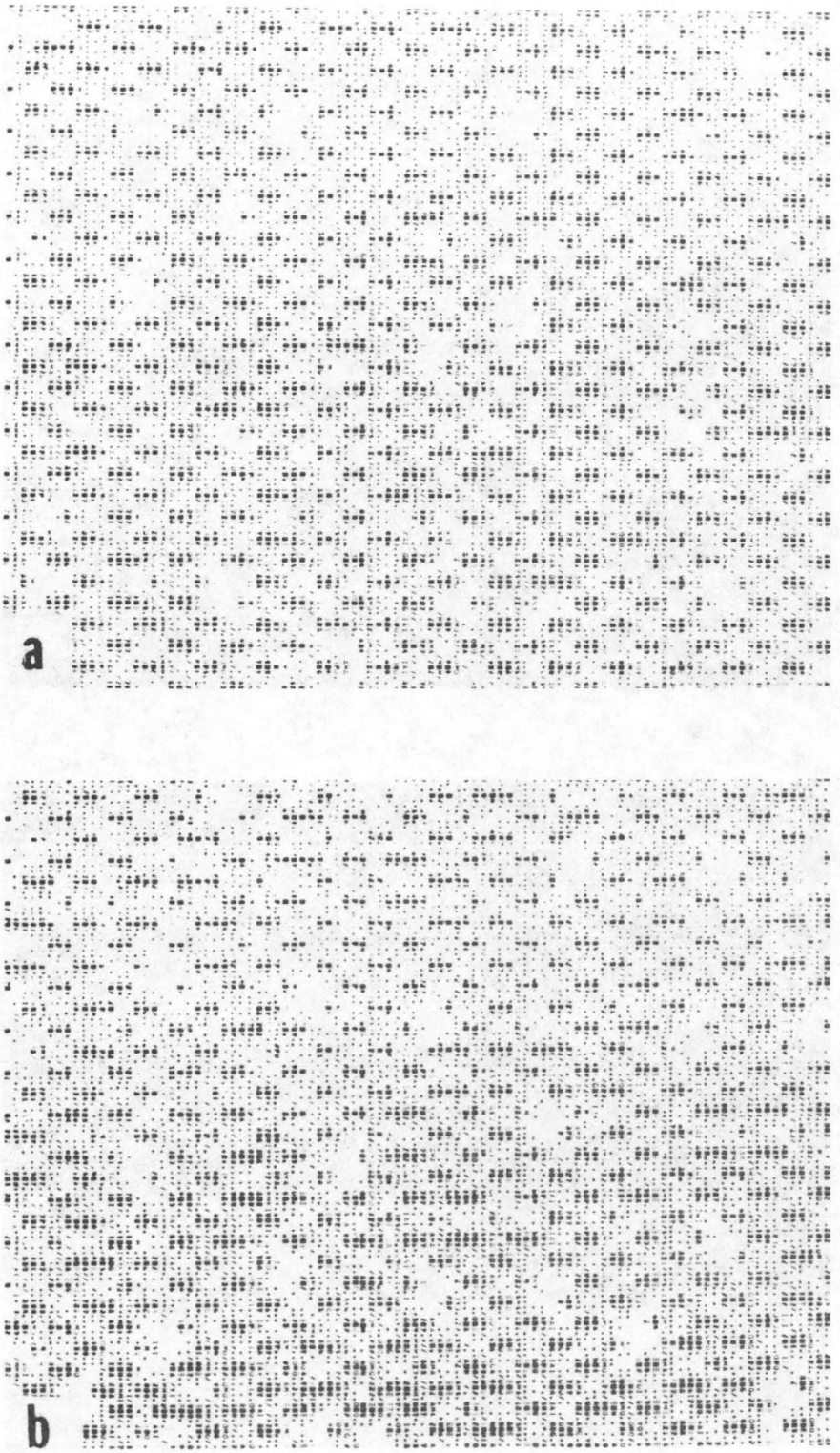

XBB 828-7380A

FIGURE 11

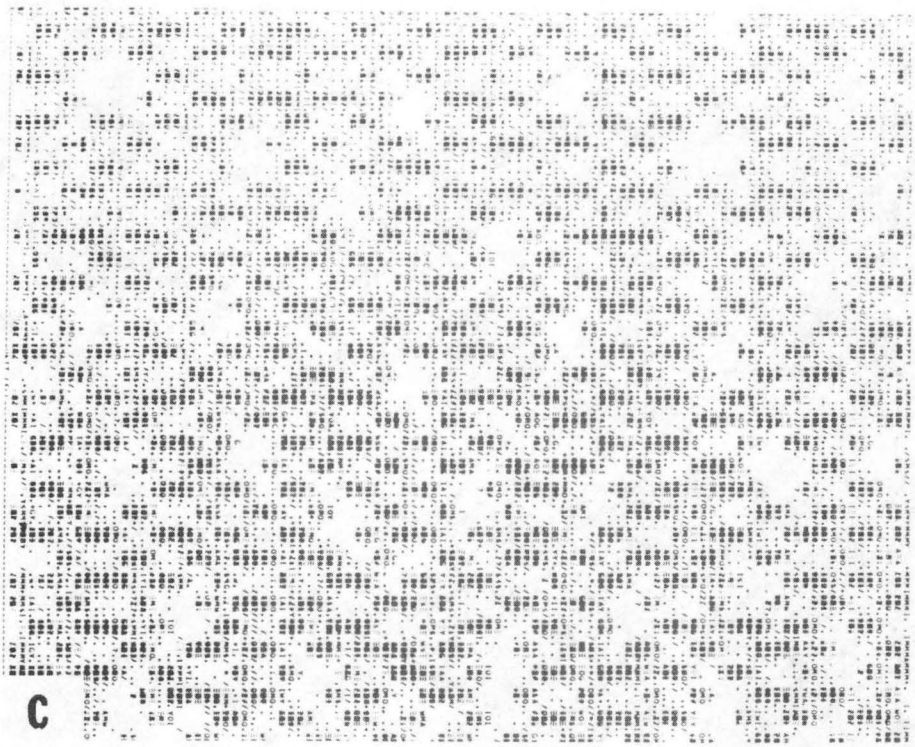

FIGURE 11 (Cont)

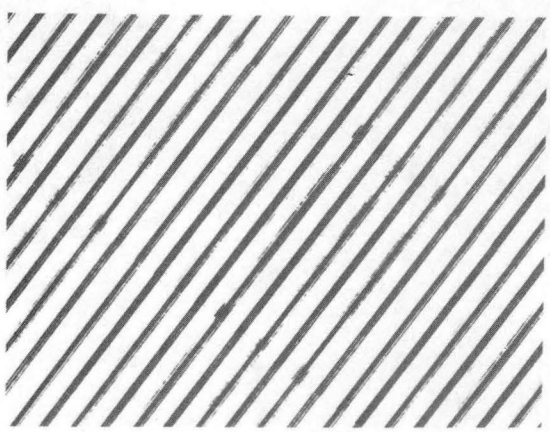

XBB 828-7383A

FIGURE 12

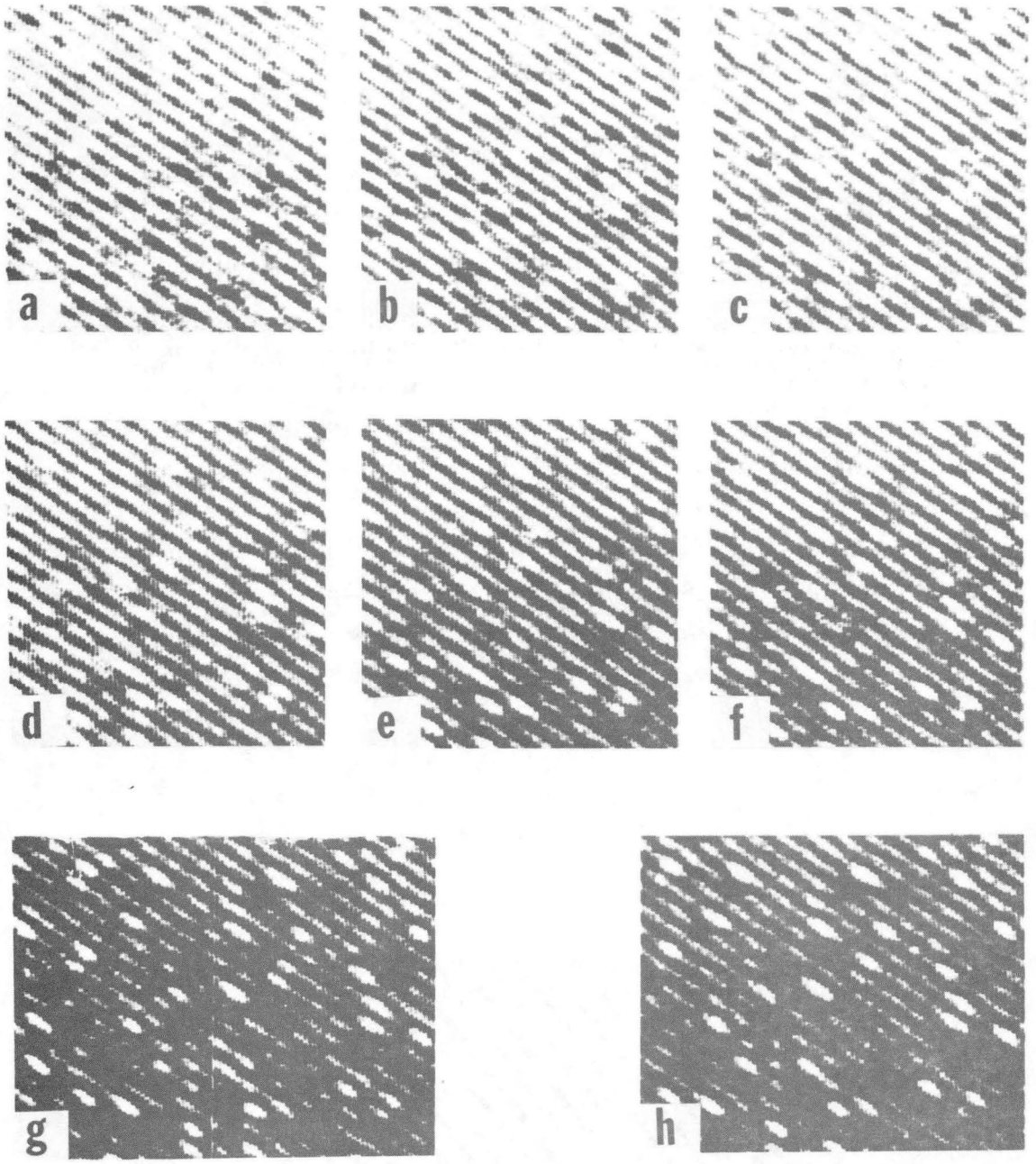

XBB 828-7385

FIGURE 13

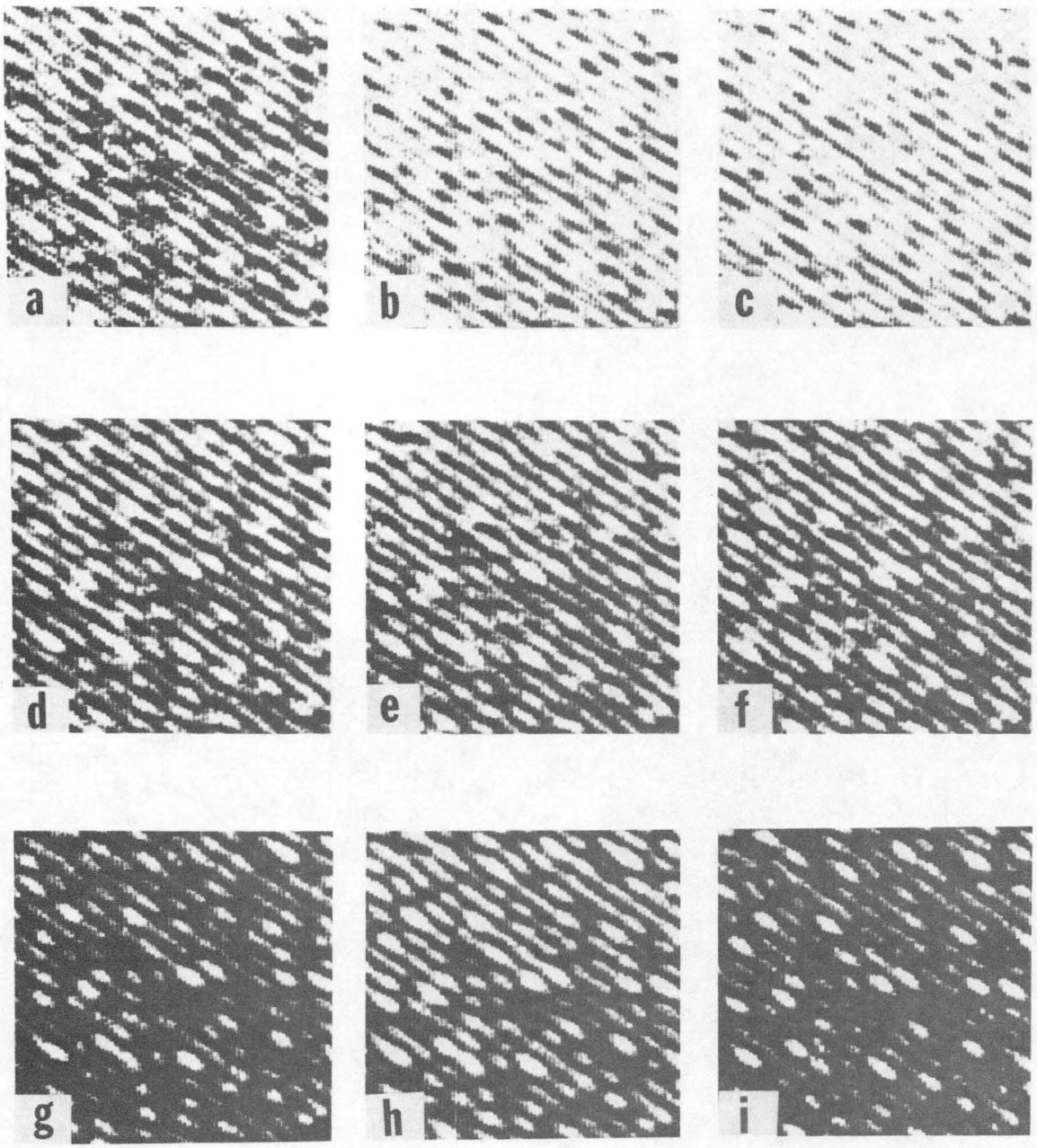

XBB 828-7381

FIGURE 14

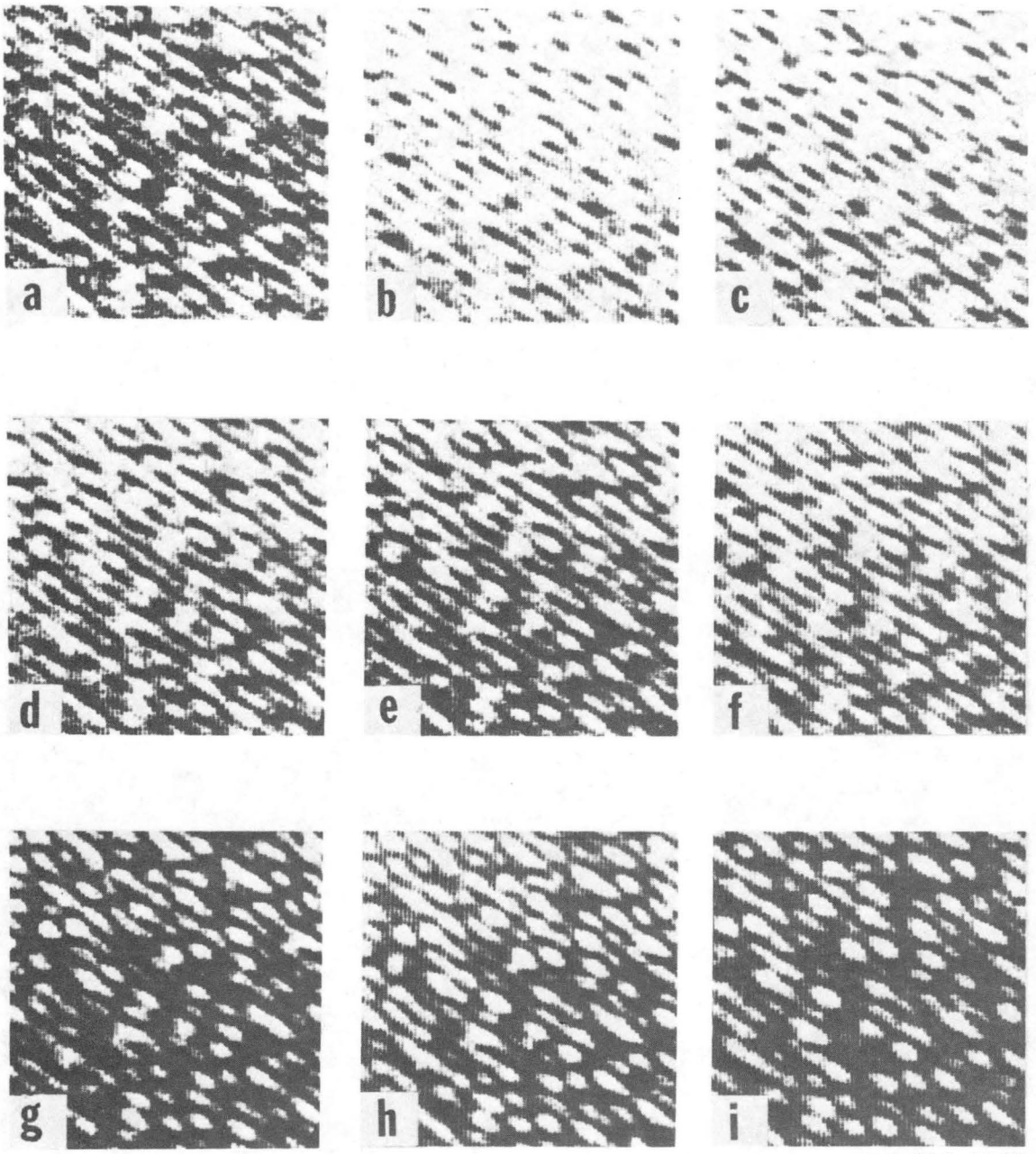

XBB 828-7384

FIGURE 15

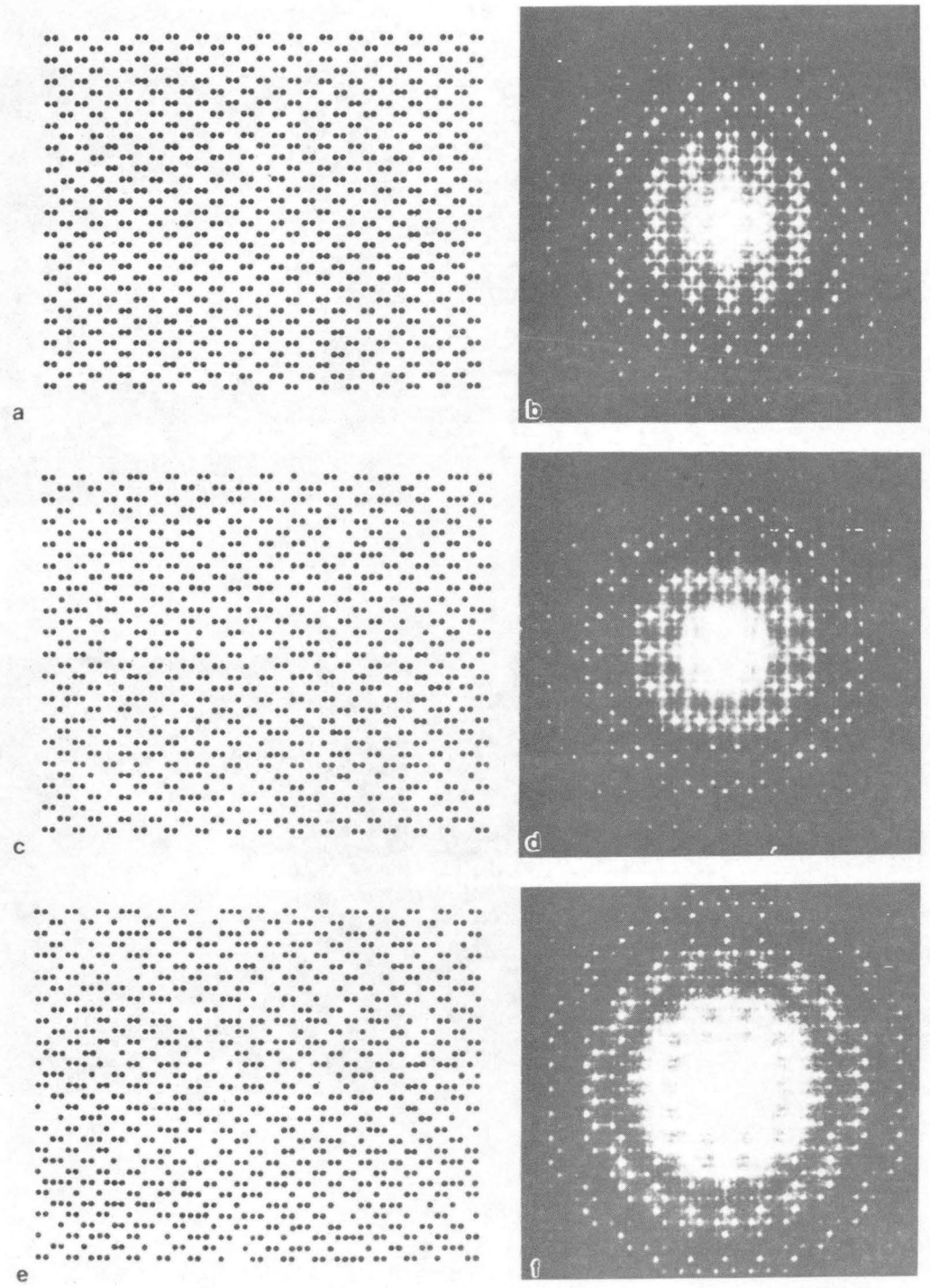

XBB 828-7067A

FIGURE 16

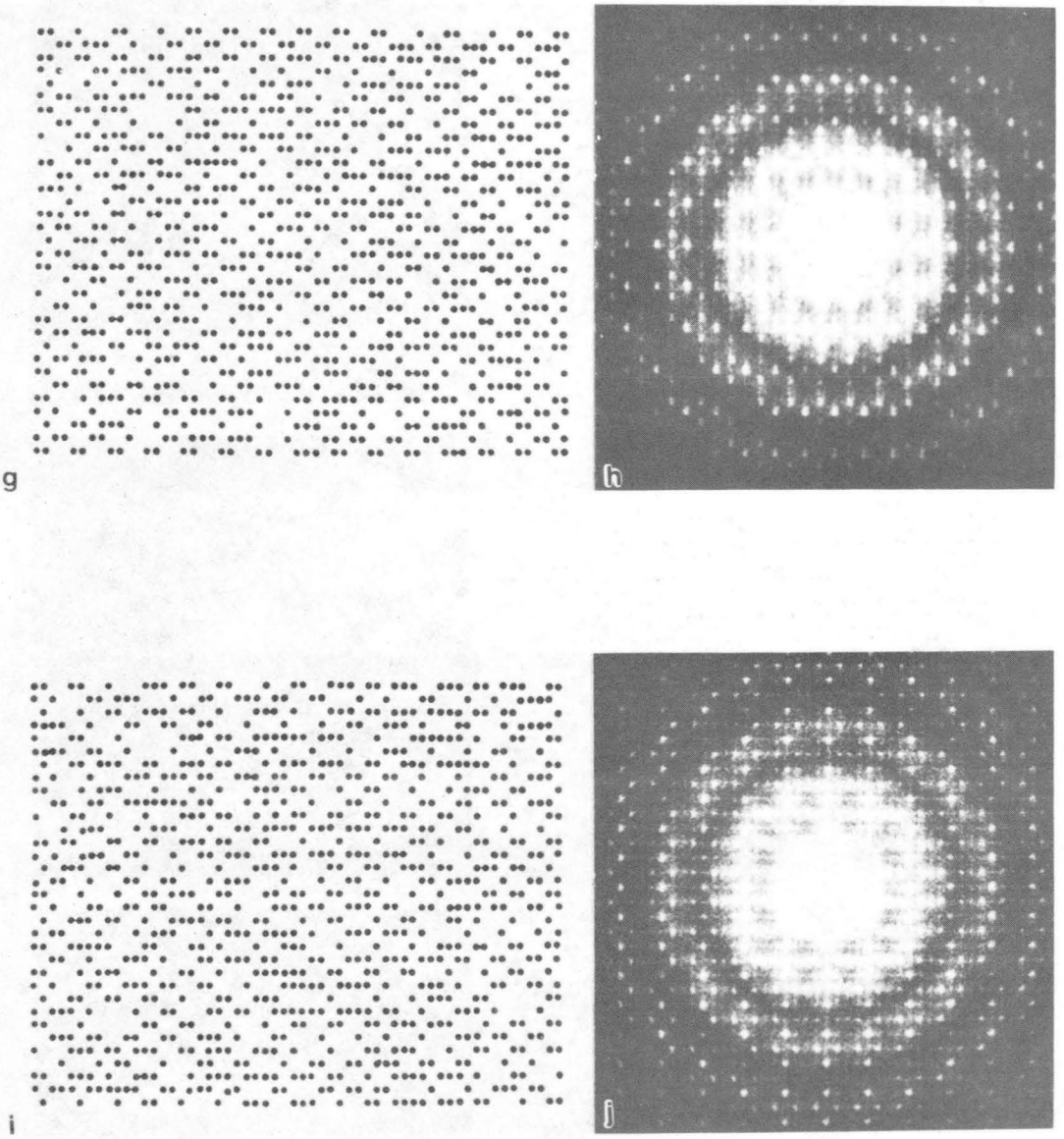

XBB 828-7066A

FIGURE 16 (Cont)

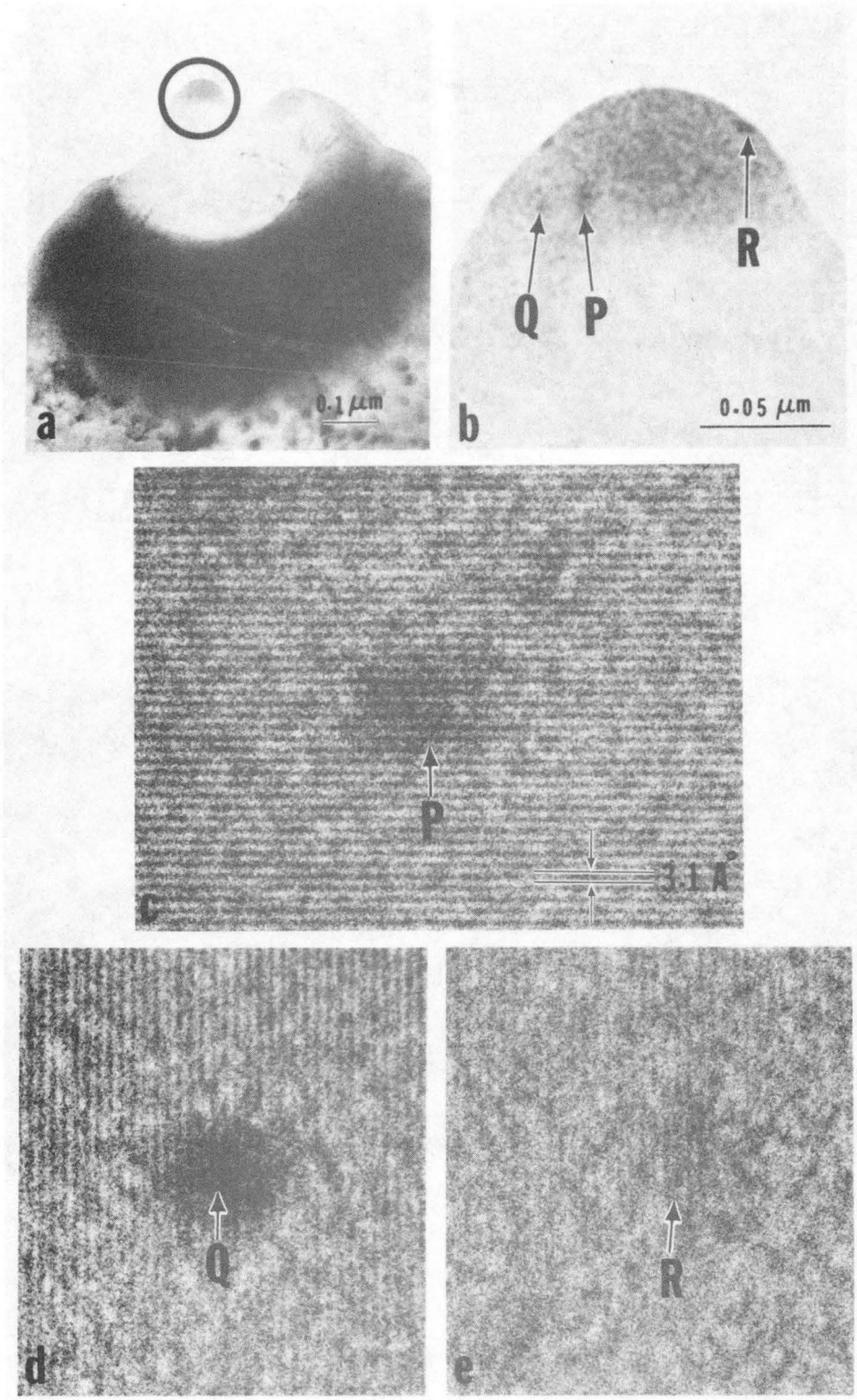

XBB 828-7389

FIGURE 17

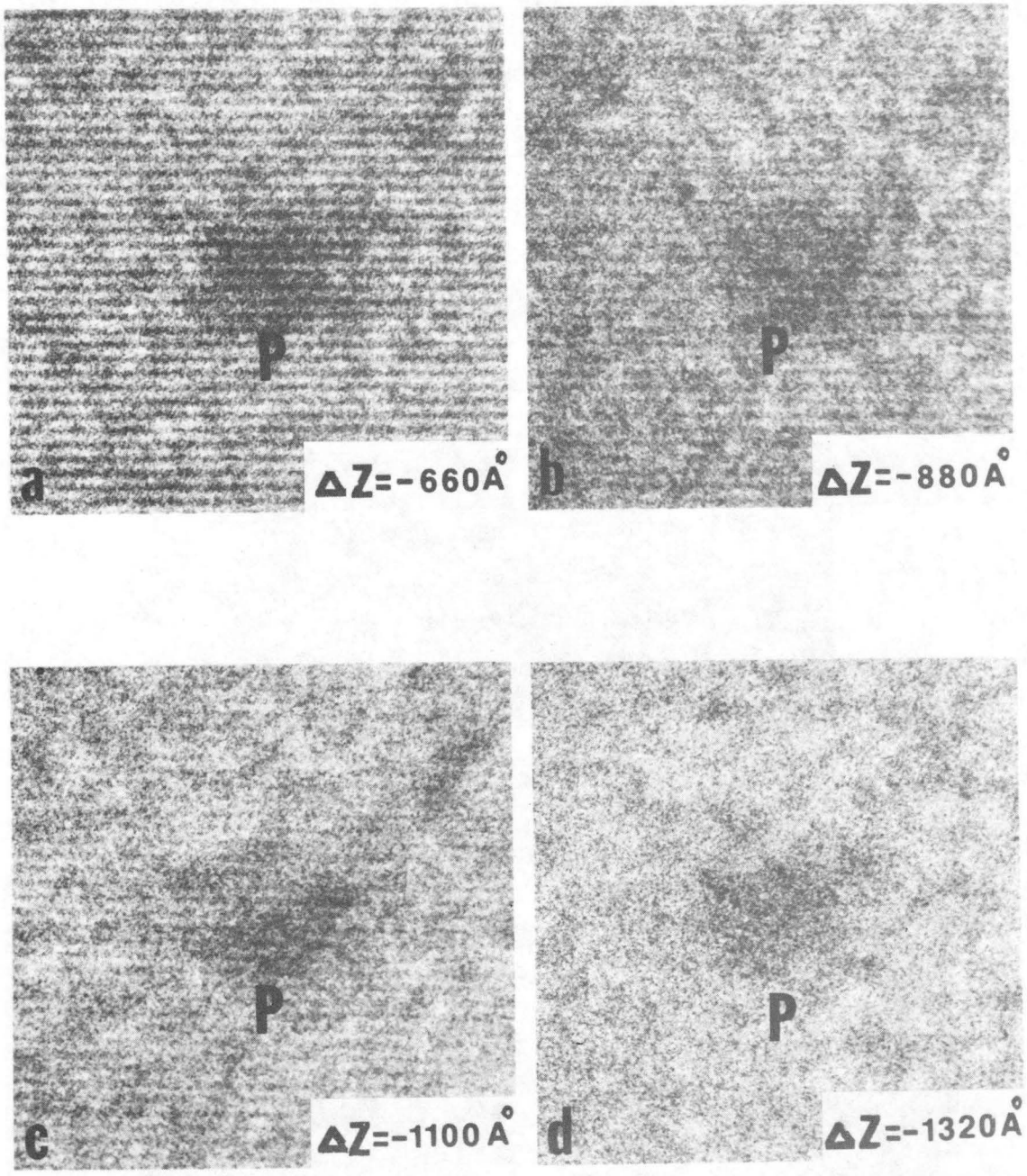

XBB 828-7388

FIGURE 18

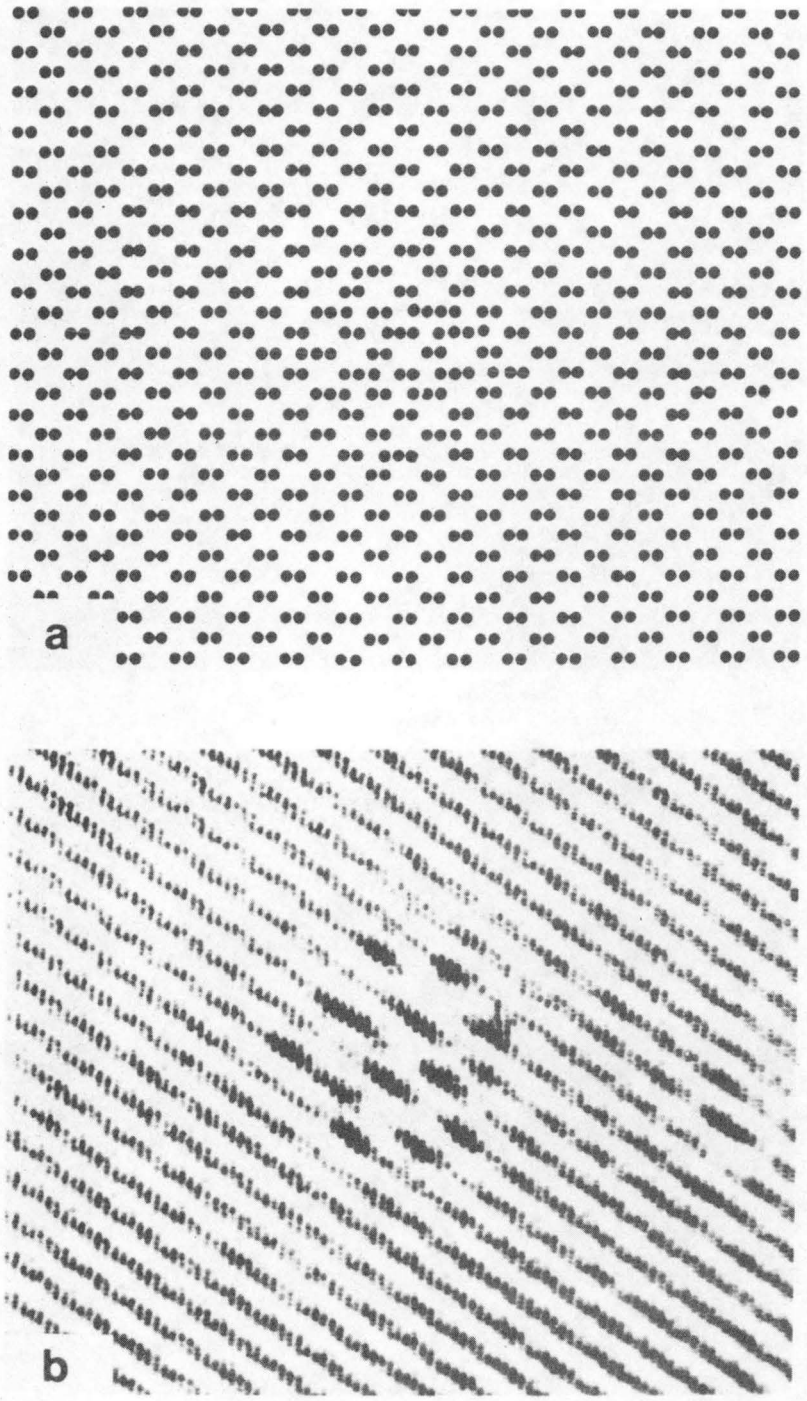

XBB 820-8794

FIGURE 19

TECHNICAL INFORMATION DEPARTMENT
LAWRENCE BERKELEY LABORATORY
UNIVERSITY OF CALIFORNIA
BERKELEY, CALIFORNIA 94720